

SPITZER AND HHT OBSERVATIONS OF STARLESS CORES: MASSES AND ENVIRONMENTS

AMELIA M. STUTZ^{1,2}, GEORGE H. RIEKE², JOHN H. BIEGING², ZOLTAN BALOG^{1,2}, FABIAN HEITSCH³, MIJU KANG^{4,5,2},
WILLIAM L. PETERS², YANCY L. SHIRLEY², MICHAEL W. WERNER⁶

Draft version October 11, 2018

ABSTRACT

We present *Spitzer* observations of a sample of 12 starless cores selected to have prominent 24 μm shadows. The *Spitzer* images show 8 and 24 μm shadows and in some cases 70 μm shadows; these spatially resolved absorption features trace the densest regions of the cores. We have carried out a ¹²CO (2-1) and ¹³CO (2-1) mapping survey of these cores with the Heinrich Hertz Telescope (HHT). We use the shadow features to derive optical depth maps. We derive molecular masses for the cores and the surrounding environment; we find that the 24 μm shadow masses are always greater than or equal to the molecular masses derived in the same region, a discrepancy likely caused by CO freeze-out onto dust grains. We combine this sample with two additional cores that we studied previously to bring the total sample to 14 cores. Using a simple Jeans mass criterion we find that $\sim 2/3$ of the cores selected to have prominent 24 μm shadows are collapsing or near collapse, a result that is supported by millimeter line observations. Of this subset at least half have indications of 70 μm shadows. All cores observed to produce absorption features at 70 μm are close to collapse. We conclude that 24 μm shadows, and even more so the 70 μm ones, are useful markers of cloud cores that are approaching collapse.

Subject headings: Dust, Extinction, ISM: Molecules, ISM: Globules, ISM: Clouds, Stars: Formation

1. INTRODUCTION

Stars are born in cold cloud cores (e.g., Bergin & Tafalla 2007), where gas and dust are compressed to high enough densities to cause the core to start collapsing. One of the most critical questions in astronomy is what the physical conditions for core formation and collapse are. Therefore, observations of cores in the rare stage during, or just prior to, collapse are critical to constrain theories of the very earliest stages of star-formation (e.g., Shu et al. 1987; Ballesteros-Paredes et al. 2003; Myers 2005).

The initial process of collapse, or the transition from a stable core to a core with an embedded protostar, happens rapidly (Hayashi 1966); additionally, the cores are necessarily dense and cold. These conditions pose significant observational challenges to identify cores close to collapse. Because of the temperature ranges involved, ~ 10 K (e.g., Lemme et al. 1996; Caselli et al. 1999; Hotzel et al. 2002), and high densities, $\sim 10^5$ cm^{-3} (e.g., Bacmann et al. 2000), cold cloud cores can best be observed at far-infrared, submillimeter, and millimeter wavelengths (e.g., Stutz et al. 2009). Such observations of dense cores show that most of them are close to equilibrium and not collapsing (e.g., Lada et al. 2008). Furthermore, if the cores are not supported by thermal and

turbulent pressure alone, then a modest magnetic field can halt collapse (e.g., Kandori et al. 2005; Stutz et al. 2007; Alves et al. 2008).

Millimeter line observations are the traditional way to search for collapsing cores (e.g., Walker et al. 1986); however, there are ambiguities in the interpretation of such measurements (e.g., Walker et al. 1988; Menten et al. 1987; Mundy et al. 1990; Narayanan et al. 1998). Here we use mid-infrared shadows as an alternative observational approach to the study of starless cores, one that does not depend on the interpretation of millimeter line profiles and how these profiles relate to the underlying velocity field of the core material. Additionally, our method is sensitive to higher column densities than traditional studies of starless cores by background star extinction, usually limited to $A_V < 30$ magnitudes (e.g., Alves et al. 2001; Kandori et al. 2005).

Cores that are isolated from regions of massive star formation are very useful to understand the initial stages of collapse into stars. These cores are free from complicating factors, e.g., massive core fragmentation, feed-back from high-mass stars, and protostellar outflows (e.g., Lada & Lada 2003; de Wit et al. 2005; Fallscheer et al. 2009), to name a few, that can have large effects on a study aimed at understanding how individual low mass stars form. We present a sample of 12 relatively isolated cores that were selected from *Spitzer* MIPS observations of Bok globules and other star-forming regions to have prominent 24 μm shadows, spatially resolved absorption features caused by the dense core material viewed in absorption against the interstellar radiation field. We also include 2 previously studied cores, CB190 (Stutz et al. 2007) and L429 (Stutz et al. 2009), for a final sample of 14 cores. Such objects with 24 μm shadows always show a counterpart 8 μm shadow, analogous to the IR absorption features produced by more distant and massive structures termed infrared dark clouds (IRDCs; e.g.,

¹ Max Planck Institute for Astronomy, Königstuhl 17, D-69117 Heidelberg, Germany; stutz@mpia.de

² Department of Astronomy and Steward Observatory, University of Arizona, 933 North Cherry Avenue, Tucson, AZ 85721, USA

³ Department of Physics and Astronomy, University of North Carolina Chapel Hill, CB 3255, Phillips Hall, Chapel Hill, NC 27599, USA

⁴ Korea Astronomy and Space Science Institute, Hwaam 61-1, Yuseong, Daejeon 305-348, South Korea

⁵ Department of Astronomy and Space Science, Chungnam National University, Daejeon 305-348, South Korea

⁶ Jet Propulsion Lab, California Institute of Technology, 4800 Oak Grove Drive, Pasadena, CA 91109, USA

Perault et al. 1996; Butler & Tan 2009; Peretto & Fuller 2009; Lee et al. 2009) and the ISO 7 μm absorption features studied by Bacmann et al. (2000). We also present Heinrich Hertz Telescope (HHT) ^{12}CO (2-1) and ^{13}CO (2-1) on-the-fly (OTF) maps of regions $\sim 10'$ on a side surrounding each core.

Our search method is efficient at identifying cores that are near collapse. In § 2 we describe the observations and data processing; in § 3 we derive optical depth maps from the 8 and 24 μm images; in § 4 we present our mass measurements and we describe the stability analysis that we apply to the sample of cores; and finally, in §5 we summarize our main conclusions.

2. OBSERVATIONS AND PROCESSING

2.1. *Spitzer* IRAC and MIPS data

The 12 cores presented here were selected from two observing programs: *Spitzer* GTO program ID 53 and GO program ID 30384. Core names, MIPS and IRAC AOR numbers, and corresponding program IDs are listed in Table 1. The IRAC data consist of observations in all four channels from programs 139 (P.I. N. Evans), 94 (P.I. C. Lawrence), and 20386 (P.I. P. Myers). The frames were processed using the *Spitzer* Science Center (SSC) IRAC Pipeline v14.0, and mosaics were created from the basic calibrated data (BCD) frames using a custom IDL program; see Gutermuth et al. (2008) for details. The MIPS observations at 24, 70, and 160 μm are from programs 53 (P.I. G. Rieke) and 30384 (P.I. T. Bourke). All observations were carried out in scan map mode and were reduced using the Data Analysis Tool (DAT; Gordon et al. 2005). These data were processed according to steps outlined in Stutz et al. (2007); please refer to that publication for further details. The data for each core are shown in Figures 1 through 12.

2.2. ^{12}CO (2-1) and ^{13}CO (2-1) Data

These cores were mapped in the J = 2–1 transitions of ^{12}CO (230.538 GHz) and ^{13}CO (220.399 GHz) with the 10-m diameter Heinrich Hertz Telescope (HHT) on Mt. Graham, Arizona. Observations taken in 2007 (CB27 and CB44) were obtained using a receiver that was a dual polarization SIS mixer system operating in double-sideband mode with a 4 – 6 GHz IF band. The observations taken after 2007 were obtained using a prototype 1.3mm ALMA sideband separating receiver with a 4 - 6 GHz IF band. The ^{12}CO (2–1) line was placed in the upper sideband and the ^{13}CO (2–1) one in the lower sideband. The spectrometers were filter banks with 128 channels of 250 KHz width and separation. At the observed frequencies the spectral resolution was $\sim 0.3 \text{ km s}^{-1}$, the band-width was $\sim 40.0 \text{ km s}^{-1}$, and the angular resolution of the telescope was $32''$ (FWHM).

The cores were mapped with on-the-fly (OTF) scanning in RA at $10'' \text{ s}^{-1}$, with row spacing of $10''$ in declination. System temperatures were calibrated by the standard ambient temperature load method (Kutner & Ulich 1981) after every other row of the map grid. Atmospheric conditions were generally clear and stable, and the system temperatures were nearly constant throughout the maps. Data for each CO isotopologues were processed with the *CLASS* reduction package (from the Observatoire de Grenoble Astrophysics Group), by removing a linear baseline and convolving the data to a

square grid with $10''$ grid spacing (equal to one-third the telescope beamwidth). The intensity scales for the two polarizations were determined from observations of standard sources made just before the OTF maps. The gridded spectral data cubes were processed with the *Miriad* software package (Sault et al. 1995) for further analysis. For each sideband the two polarizations were averaged together yielding the map RMS noise levels listed in Table 2; also listed are the map center coordinates, dates of observation, sizes, system temperatures, and velocity ranges which include significant emission. The ^{12}CO and ^{13}CO integrated intensity images, integrated over the velocity ranges listed in Table 2, are shown in Figures 13 through 15; these images are centered on the 24 μm shadow coordinates.

3. ANALYSIS

3.1. Optical Depth Maps

In this section we calculate the 24 μm and 8 μm optical depths for the shadow features seen in Figures 1–12. We assume that the cores are optically thin and that there is no foreground emission originating from the surface layers. We apply an analysis analogous to that presented in Stutz et al. (2007) at 24 μm and Stutz et al. (2008b) at 8 μm ; however, we update the analysis presented in that work with a more robust calculation of the unobscured background flux level (f_0 in what follows).

3.1.1. 24 μm Optical Depth Calculation

Under the above assumptions, the optical depth at 24 μm is

$$\tau_{24} = -\ln \left(\frac{f' - f_{\text{DC}}}{f'_0 - f_{\text{DC}}} \right). \quad (1)$$

Here f_{DC} is the contribution to the image flux level of all foreground sources, such as zodiacal emission and instrumental background; f' and f'_0 are the shadow flux and the intrinsic, unobscured flux, respectively. In what follows f and f_0 indicate the DC-subtracted values of the shadow fluxes: $f = f' - f_{\text{DC}}$ and $f_0 = f'_0 - f_{\text{DC}}$. The contribution of f_{DC} to the overall image flux level is assumed to be constant over image areas large compared to the size of the shadow while f_0 is determined in the region immediately adjacent to the shadow. Further details on the determination of these two quantities is provided in the following discussion. However, before proceeding, we note that the shadow depth, or contrast, in the absence of foreground emission from the surface of the shadow itself, is the result of the depth of the absorption feature relative to the quantity $(f'_0 - f_{\text{DC}})$; a stronger background allows for robust sensitivity to larger τ . Furthermore, an over-estimate of f_{DC} will artificially boost the shadow contrast and cause an over-estimate of τ and all dependent quantities. Rather than following the procedure applied in Stutz et al. (2009), where the darkest region of the L429 shadow was used to measure f_{DC} , the approach implemented here takes advantage of dark regions in the *Spitzer* images which are not associated with any absorption features. These regions provide an independent estimate of the foreground emission; furthermore, when shadow pixels are darker than, or have a lower value than, the f_{DC} level, we exclude them from our analysis because they are most likely not sensitive to the total column of material in that pixel, i.e., they have become saturated.

Image DC level (f_{DC}) determination. To measure f_{DC} , we select regions in the $24\ \mu\text{m}$ image with no diffuse emission. These regions also have little to no detected emission at 70 and $160\ \mu\text{m}$. As a further check on the cleanliness of the background estimate, when possible we select the background region to overlap partially with, or be adjacent to, ^{12}CO and ^{13}CO map areas that are free from molecular line emission. Additionally, we avoid the areas near the edges of the images due to poor signal-to-noise and sparse coverage. The background region box size is $5'$ on a side, corresponding to $\sim 59,000$ mosaic pixels, which are subsampled by 2×2 relative to the physical pixels. We set f_{DC} equal to the 0.5 percentile pixel value; as discussed above, this low value is conservative because a higher value may over-estimate the shadow contrast relative to f'_0 . The error in f_{DC} , σ_{DC} , is determined by simulating $\sim 59,000$ pixels drawn from a normal distribution with the same mean and standard deviation as the background region; the 0.5 percentile pixel value is stored and the process is repeated 10^4 times. The standard deviation of the resulting distribution values is our estimate of σ_{DC} (Stutz et al. 2007). The pixel error map for the background subtracted images is then calculated using the DAT (Gordon et al. 2005) pixel error map, multiplied by a factor of 2 to take into account pixel-to-pixel correlations due to the sub-sampling, with σ_{DC} added in quadrature.

Unobscured flux (f_0) determination. We apply iterative Gaussian fitting to the image pixel value distributions to estimate f_0 , the local, unobscured flux near the shadow, similar to the method developed by Stutz et al. (2008a) to reconstruct and analyze the noise properties in deep *Hubble* Space Telescope ACS images. In summary, we adjust the upper cutoff of the pixel value distribution so that the Gaussian fit is least affected by the non-Gaussian tail of the high pixel value distribution. This is done by finding the upper pixel value cutoff that has the narrowest Gaussian width. This fitting method is constructed to minimize the effects of sources or shadows on the estimate of f_0 . We proceed by constructing a pixel value histogram for all pixels within r_0 of the shadow using a bin size of $0.4\ \mu\text{Jy}/\text{arcsec}^2$. We then clip the distribution by excluding all bins with values below the mean pixel value in a $30''$ radius aperture centered on the shadow. The shadow pixel-value distribution in this region is indicated as a grey histogram in Figures 16–19; the mean value of the shadow flux is indicated with a solid line. Excluding these bins avoids a possible bias of the best-fit mean pixel value towards lower values. Next we fit the histogram data to an unweighted Gaussian model, using standard IDL packages, and excluding all bins with values greater than the maximum bin plus one. We repeat this fitting procedure as we include successively higher value bins one at a time. The resulting best-fit Gaussian width (σ) values are shown in Figures 16–19 in the lower-left panel for each object, plotted as a function of the maximum bin value included in the fit. The solid line indicates the minimum σ from the distribution of Gaussian widths; the mean value of the fit corresponding to the minimum value of sigma is the adopted value of f_0 . These two parameters are listed in the figure.

To determine the effect the choice of pixel histogram radius (r_0) has on our derived value of f_0 we repeat this

procedure over a range of r_0 values from $r_0 = 60''$ to $300''$, in $20''$ steps; the resulting values of f_0 and σ are shown in the right-hand-side panel of Figures 16–19. In most cases the f_0 profiles flatten out by $r_0 = 240''$, as indicated by the dashed line. This value is used for all objects except CB42, which lies near the edge of the MIPS mosaic; since the f_0 profile for CB42 appears to flatten out by $140''$, the largest value of r_0 that we test for this core, we assume this value is valid. In the cases of CB26 and CB27 we do not measure as abrupt a flattening. For these cores we still use $r_0 = 240''$ as a conservative estimate; larger values for r_0 may over-estimate f_0 and the derived optical depths. Furthermore, ideally we calculate f_0 as close as possible to the shadow features; as the distance from the core is increased, other effects can bias the determination of f_0 , such as diffuse emission not associated with the core. We estimate the uncertainty in f_0 to be $\sigma(f_0) = 0.02 \times f_0$. The Gaussian error in the mean gives a SNR for f_0 of $\gtrsim 230$ for all cores; we consider this SNR to be optimistic.

Using our calculated value of f_0 and the background subtracted image, we calculate τ_{24} in each pixel and the associated error $\sigma_{\tau,24}$, using standard propagation of errors, including σ_{DC} and $\sigma(f_0)$. The pixel-to-pixel correlations are significant and we do not take this into account in the τ pixel error maps; consequently, the error maps underestimate the true errors and we do not use them in the subsequent analysis. In the cases where the values of f near the center of the cores are negative, causing τ_{24} to diverge, we set the value of τ_{24} equal to the mean $\langle \tau_{24} \rangle$ in an aperture with radius $10''$ or larger, depending on the size of divergent region, centered on the core. For most (8/12) cores, the number of divergent pixels is less than 90, corresponding to an effective circular area with radius smaller than $6''.5$; for objects CB130 and CB180 the divergent region has an effective radius of $\sim 7''.5$, for CB44 the region has a radius of about $25''$, and for L1552 the region radius is about $20''$. This approach is conservative when analyzing core stability because it effectively underestimates the $24\ \mu\text{m}$ shadow masses. Furthermore, an alternative approach is to estimate f_{DC} as a fraction of the shadow pixel values; while this method would circumvent the divergent pixel issue, it would yield larger core masses, potentially biasing our collapse analysis. The divergent pixels found with our method are flagged and accounted for in the subsequent analysis. The $24\ \mu\text{m}$ τ pixel maps are shown in the left column of Figures 13 through 15.

3.1.2. $8\ \mu\text{m}$ Optical Depth Calculation

We apply the same techniques described above for the $24\ \mu\text{m}$ images to the $8\ \mu\text{m}$ images, with the exceptions described here⁷. The results are illustrated in Figures 20–23. For the f_{DC} determination, it is not possible to use the same regions as those used for the $24\ \mu\text{m}$ images because of the limited coverage of the $8\ \mu\text{m}$ images; therefore we select new regions that are near the $24\ \mu\text{m}$ regions when possible. In all cases the $8\ \mu\text{m}$ f_{DC} regions are selected to include the darkest regions of the image; we set f_{DC} equal to the 0.1 percentile. The background region box size is $5'$ on a side, corresponding to $\sim 60,000$ pixels at the plate scale of the IRAC images

⁷ There is no IRAC coverage of source CB42

($1''.22 \text{ pix}^{-1}$). The $8 \mu\text{m}$ error is assumed to be 2% of the pixel flux value; the background error is estimated as described above. These two quantities added in quadrature make the background-subtracted pixel error map. The method used to determine f_0 is identical to that described above, the only exception being that for some objects (CB23, L1544, L492, and L694-2) the maximum radius for which we can measure the pixel value distribution is limited by the size of the images. For these four objects, we chose the largest radius measurement of f_0 for which over 50% of the area of the annulus contains image pixels. For these cores the maximum radius is $r_0 = 240''$ for CB230, and $r_0 = 200''$ for the rest. For cores with sufficiently large images, we observe a flattening of the f_0 profiles at a radius of $r_0 = 260''$; the adopted values for r_0 are indicated as dashed lines in the right column of Figures 20–23. In the cases of cores CB23 and CB27, we do not observe a flattening; therefore the τ_8 maps for these sources may be less reliable.

As described above for the $24 \mu\text{m}$ images, we use our measurements of f'_0 , f' , and f_{DC} measured from the $8 \mu\text{m}$ images to calculate

$$\tau_8 = -\ln\left(\frac{f' - f_{\text{DC}}}{f'_0 - f_{\text{DC}}}\right)$$

in each pixel; we also calculate $\sigma_{\tau,8}$ with standard propagation of errors and including σ_{DC} and $\sigma(f_0)$, where $\sigma(f_0) = 0.02 \times f_0$. Divergent pixels are assigned a value according to the procedure outlined above, are flagged, and are accounted for in subsequent analysis.

We detect $3.6 \mu\text{m}$ emission above the sky level in a large fraction of our cores (TMC1-1C, CB23, CB26, CB27, L1544, L1552, and L694-2, and marginally in L492, CB130, and CB180). This emission is spatially coincident with the shadows, and similar in extent to the $160 \mu\text{m}$ emission. The lack of any significant $8 \mu\text{m}$ aromatic feature indicates that this emission is likely to be caused by the surface layer of dust grains scattering the interstellar radiation field, analogous to the near-IR emission studied by Lehtinen & Mattila (1996). Such near-IR emission has been used to study interstellar clouds (e.g. Foster & Goodman 2006; Padoan et al. 2006; Nakajima et al. 2008). Juvela et al. (2008) show that when using J , H , and K_S imaging this technique is sensitive to densities of $1 \lesssim A_V \lesssim 15$ magnitudes. Including the $3.6 \mu\text{m}$ emission might increase the densities accessible to this technique, as well as providing a high-spatial resolution shadow-independent extinction estimator. We note that for the cores L1544, CB44, and L694-2 the emission shows a limb-brightening geometry at $3.6 \mu\text{m}$, where the center of the shadow region appears darker than the surrounding region.

The $8 \mu\text{m}$ shadow determinations provide a test of the validity of those at $24 \mu\text{m}$. In all cases where a good comparison is possible, the agreement is satisfactory if we take the optical depths at the two wavelengths to be approximately equal, $\tau_{24}/\tau_8 = 1.0 \pm 0.1$ (see also Flaherty et al. 2007; Chapman et al. 2009; Chapman & Mundy 2009). Additional details will be provided in a future publication.

3.2. Distance measures

Here we make some remarks on our adopted distances, which are summarized in Table 3.

TMC1-1C, CB23, CB26, CB27, L1544, L1552 — Kenyon et al. (1994) derive a distance to the northern portion Taurus of 140 ± 10 pc based on extinction of background stars. This distance is roughly consistent with recent determinations using trigonometric parallax with the VLBA (Torres et al. 2009).

CB42 — We find no distance estimate for this source in the literature. In the direction of CB42, the extent of the local bubble is ~ 100 pc (Lallement et al. 2003); we adopt a distance of 100 pc, a conservative lower limit distance.

CB44 — Hilton & Lahulla (1995) list the Bok & McCarthy (1974) assumed distance of 400 pc. They also list the Tomita et al. (1979) estimate of 300 pc, and the Arquilla & Goldsmith (1986) distance estimate of 400 to 600 pc. We adopt a distance of 400 pc.

L492, CB130 — Straizys et al. (2003) investigate the distance dependence of the interstellar extinction in the direction of the Aquila Rift. These authors find that the distance is 225 ± 55 pc to the front edge and that the cloud has a depth of about 80 pc. Because these cores are viewed in absorption they are unlikely to be located behind much cloud material; therefore we adopt 225 pc as the distance to these cores.

CB180 — Hilton & Lahulla (1995) list the Bok & McCarthy (1974) assumed distance of 400 pc. Bok & McCarthy (1974) do not elaborate on their adopted distances. This object is near the Scutum association. We adopt 400 pc for the distance to this core.

L694-2 — Kawamura et al. (2001) derive a distance of 230 ± 30 pc using star counts.

4. DISCUSSION

4.1. Interpretation of Collapsing Cores

The stability of a cloud core is usually deduced through observations of millimeter-wave molecular emission lines (e.g., Gregersen et al. 1997; Mardones et al. 1997; Gregersen & Evans 2000; Crapsi et al. 2005; Williams et al. 2006; Sohn et al. 2007), but the dynamical state of these lines can be affected by rotation, turbulence, optical depth, and other effects that can hide or mimic the indicators for collapse. We use infrared shadows, together with millimeter-wave spectroscopy, as an alternative, complementary, and reliable indicator of impending collapse (e.g., Stutz et al. 2007, 2009). These observational techniques can be used to estimate the masses and dynamical states of the cores. Conventionally, collapse is identified by fitting such observations to Bonnor-Ebert model profiles which assume spherical symmetry (e.g., Evans et al. 2001; Ballesteros-Paredes et al. 2003; Shirley et al. 2005). However, as shown in Figures 1 through 12, few of our objects appear symmetric on the plane of the sky, calling the applicability of this approach into question.

Instead, we have probed the collapse state of these cores on the basis of a simple Jeans mass calculation. In what follows, we determine $24 \mu\text{m}$ core masses and sizes. Given these core properties, and assuming a temperature of 10 K (reasonable for starless cores) we derive

a Jeans mass for each core:

$$M_J = \left(\frac{5kT}{G\mu_p m_H} \right)^{3/2} R^{3/2} M^{-1/2}, \quad (2)$$

where M is the 24 μm core mass (M_{24}^{core} in Table 4), R is the effective radius of the core ($R_{\text{eff}}^{\text{core}}$ in Table 4), measured from the 24 μm image, and we have assumed that the mean molecular mass per free particle μ_p is equal to 2.4. The sizes of the cores are derived from the area in which we detected the 24 μm shadows (see § 4.2.1). We note that assuming a temperature of 8 K or 12 K for these cores cause a $\sim 30\%$ change in the calculated Jeans mass. The distance dependence of the Jeans mass is $D^{1/2}$. In the following analysis (see Tables 4 and 5) we compare shadow masses, with a distance dependence of D^2 , to the Jeans mass. We caution that the ratio of the 24 μm masses to the Jeans mass has a steep distance dependence of $D^{3/2}$. This Jeans mass analysis avoids possible biases introduced by imposing more stringent geometrical assumptions in the core analysis. However, it only takes thermal support into account.

Under more realistic conditions, turbulence might also provide support against collapse. From Hotzel et al. (2002), the energy contributed by turbulence to the support of the cloud is

$$E_{\text{turb}} = \frac{\mu_p}{AMU} \left(\frac{\Delta V^2}{\Delta V_{\text{th}}^2} - 1 \right) E_{\text{th}}, \quad (3)$$

where AMU is the atomic mass number of the species from which we measure the observed line width ΔV , and ΔV_{th} is the expected thermal line width for that species, assuming a temperature of 10 K. To estimate possible contributions of turbulence to the support in the cores, we use previously measured ΔV values for high density tracers from the literature when available (e.g., Lee et al. 2004; Crapsi et al. 2005; Sohn et al. 2007). When such measurements are not available, we use other line widths as estimators, noting that lower density tracers will overestimate the line width and therefore the contribution from turbulence to the support. Often, the turbulent support is much less than the thermal support and hence can be ignored in considering the stability against collapse. In the cases where turbulent support is potentially significant, we attempt to assess its contribution relative to the Jeans mass and magnetic field required for stability.

Magnetic fields may also contribute to the support. The inferred magnetic field strengths in cores range from $\lesssim 15 \mu\text{G}$ to $\sim 160 \mu\text{G}$ (Bergin & Tafalla 2007). From Stahler & Palla (2005), given a magnetic field strength B and a cloud radius R , the mass that can be supported is

$$M = 70M_{\odot} \left(\frac{B}{10\mu\text{G}} \right) \left(\frac{R}{1\text{pc}} \right)^2. \quad (4)$$

Using this relation, and a measurement of the core mass and size, we estimate the minimum magnetic field strength required to support the core. If the cores require field strengths above $\sim 160 \mu\text{G}$, we consider it unlikely that the core is supported by a magnetic field. Furthermore, if the minimum magnetic field derived in this fashion is reasonable, but the core mass is significantly greater than the Jeans mass (by a factor $\gtrsim 2$), we

consider it unlikely that the core is stable against collapse. Our understanding of the magnetic field strengths in cores does not allow for strong constraints. However, this qualitative assessment gives a useful estimate of the possible role of the magnetic field.

Finally, rotation can also contribute to the support in cores. In column 9 of Table 4 we list the rotational velocity required to fully support our sample of cores. Future high-resolution observations will determine the extent of the role of rotation in these cores. In the analysis that follows, we interpret the line widths as caused only by turbulent and thermal motions; more realistically, turbulent motions on large scales can be confused with rotation (Burkert & Bodenheimer 2000). Furthermore, irregular infall, or fragments, can mimic turbulence; inspection of Figures 1 through 12 reveals that a significant fraction of cores have geometries which are not regular, reminiscent of structures seen in self-gravitating 2D (Burkert & Hartmann 2004) and 3D (Heitsch et al. 2008) simulations. Because of these irregular shapes, we have attempted to minimize geometrical assumptions in the analysis of our sample of cores, as discussed above; however, the stability arguments applied here inherently still assume approximate sphericity.

4.2. Mass Measurements

We describe the method used to calculate masses in the cores using the 24 μm shadows, and in the regions surrounding the cores using the ^{12}CO and ^{13}CO data. The results are summarized in Table 4. We also list the Jean mass for each core, assuming all the cores are at a temperature of 10 K and that the core density is described by the shadow mass (M_{24}^{core}) and the effective radius ($R_{\text{eff}}^{\text{core}}$; see below).

4.2.1. Core Masses: Shadow Masses

We calculate masses in the cores applying a similar method as that of Stutz et al. (2007). Core shadow masses, assumed distances, and effective areas are listed in Table 4. In these calculations, we use the 24 μm images and 8 μm dust opacities from Ossenkopf & Henning (1994): $\kappa_8 = 1.21 \times 10^3 \text{ cm}^2 \text{ gm}^{-1}$ for thick ice mantles at a density of 10^6 cm^{-3} . This choice of dust opacity is motivated by our analysis in § 3.1.2 where we find that $\tau_{24/8} = \tau_{24}/\tau_8 = 1.0 \pm 0.1$. This choice of Ossenkopf & Henning (1994) dust model has a ratio of $\tau_{24}/\tau_8 = 1.1$, close to our measured value.

The mass in a region with an optical depth τ_{24} is:

$$M_{24} = \frac{\Omega D^2}{\kappa_8} \alpha \times \tau_{24}, \quad (5)$$

where Ω is the solid angle subtended by the region, D is the distance, $\alpha (= 100)$ is the assumed gas-to-dust ratio, and κ is the assumed dust opacity. We measure the mean flux in an aperture of 1.5 radius, excluding all pixels that have $\tau_{24} \leq 0.0$ in the maps described above. Using the measurements of f_{DC} and f_0 and the mean flux per pixel in the shadow, we then calculate the mean τ_{24} per pixel. Using equation 2 and the number of pixels ($\Omega = N_{\text{pix}} \times \text{pixel scale}^2$) included in the mean flux calculation we calculate a shadow mass. We use the value of Ω in subsequent analysis as a measure of the effective core sizes, where $R_{\text{eff}}^{\text{core}} = \sqrt{\Omega/\pi}$. The uncertainties

in the masses measured in this fashion are of order 15%, without including distance uncertainties. We cross-check these masses by calculating core masses directly from the τ -pixel maps. We find that the two sets of masses agree well; however, the mass errors are extremely low for the τ -pixel map masses. We attribute this discrepancy to highly correlated errors, as discussed in § 3.1, and disregard the small uncertainties in favor of the $\sim 15\%$ errors. The agreement between the two masses indicates that the method we use to estimate f_{DC} (see § 3.1.1) does not have a large effect on the calculated core masses, even accounting for divergent pixel values.

4.2.2. Envelope Masses: Molecular Masses

We use the ^{12}CO (2–1) and ^{13}CO (2–1) maps to derive the total column density of hydrogen, $N(\text{H})$ in the area surrounding the cores. As listed in Table 2 and shown in Figures 13 through 15, the CO maps cover areas that are much larger than the $24\ \mu\text{m}$ shadow area. The effect of CO freeze-out onto dust grains is severe (Bacmann et al. 2002; Tafalla et al. 2002); therefore, in the area where we observe $24\ \mu\text{m}$ shadows, the column densities derived from CO observations are likely to be underestimated. However, in the regions outside of the shadows, where the densities are much lower than in the cores themselves, the CO-derived $N(\text{H})$ column should have a much higher degree of fidelity to the true column in the observed region. Therefore, we use the CO maps to derive masses of the larger environment surrounding the cores, observed as $24\ \mu\text{m}$ shadows⁸.

To derive masses from the CO data, we follow a similar procedure as Povich et al. (2009) (see also Kang et al. 2009) and we apply the escape probability radiative transfer model for CO from Kulesa et al. (2005). The ^{12}CO (2–1) and ^{13}CO (2–1) data cubes are used to derive the column of CO in each $10'' \times 10''$ map pixel, assuming an isotope ratio of $^{12}\text{CO}/^{13}\text{CO} = 50$. The model uses the ^{12}CO and ^{13}CO observations to solve for the column density of CO, $N(\text{CO})$, over a model grid of temperatures, densities, and column densities; given an initial guess for the density this procedure then fits simultaneously for the temperature and column density in each map pixel. The mass calculation also incorporates the van Dishoeck & Black (1988) PDR photodissociation model of CO, intended to account for the effect of the far-UV field, G_0 , incident on the cores. The final CO column that we calculate therefore should include the effect of UV dissociation; if the UV-field is not strong, the application of this model can cause an over-estimate of the column densities.

After calculating the total (atomic plus molecular) column $N(\text{H})$ in each pixel, we derive masses using the distances collected from the literature (listed in Table 3 and discussed in § 3.2). We calculate total cloud masses by integrating the $N(\text{H})$ pixel distribution over a $4'$ radius aperture centered on the shadow, indicated as $M_{\text{CO},4}$ in Table 4. The left column of Figures 24 through 27 show the ^{13}CO integrated intensity maps (grey scale) with the

calculated $N(\text{H})$ column density contours overlaid; we find good spatial agreement between the two. The right column of Figures 24 through 27 shows the ^{12}CO and ^{13}CO spectrum averaged over the $r < 1.5$ shadow region and in the $4' > r > 1.5$ annulus where the dotted lines indicate the velocity range used to calculate the column density $N(\text{H})$. We also calculate molecular core masses over a circular aperture of size equal to the effective area of the core derived from the $24\ \mu\text{m}$ τ maps ($M_{\text{CO}}^{\text{core}}$); the effective radii ($R_{\text{eff}}^{\text{core}}$) range from 1.2 to 1.4 for this sample of cores and are listed in Table 4.

4.3. Results

We use our optical depth maps at 8 and $24\ \mu\text{m}$, τ_8 and τ_{24} , to derive core masses; we use the ^{12}CO and ^{13}CO maps to measure the mass of material in the larger environment surrounding the cores. We then compare the Jeans mass criterion and other information to assess the collapse status of each core. Here we summarize our results:

TMC1-1C: Our analysis shows that this core is stable, assuming only thermal support. It is therefore highly unlikely that this core will collapse soon given its current configuration. If the mean density in the core increases by $\sim 20\%$ the core will exceed the Jeans mass criterion; if that happens and if magnetic and turbulent support are negligible then eventually collapse will take place. Kauffmann et al. (2008) use the MAMBO bolometer array to observe the thermal dust continuum emission at 1.2 mm. In their study this shadow is designated as TMC1-1C 3C, with a measured mass of $10.71 \pm 0.07 M_{\odot}$, in good agreement with our CO-measured mass of $11.4 M_{\odot}$. Crapsi et al. (2005) measure the N_2H^+ (2–1) and N_2D^+ (2–1) line widths to be 0.21 and 0.13 km s^{-1} , respectively; they do not measure a large $\text{N}_2\text{D}^+/\text{N}_2\text{H}^+$ ratio and do not classify this source as very advanced chemically or in evolution. Caselli et al. (2008) measure the ortho- H_2D^+ ($1_{1,0}-1_{1,1}$) emission, which is likely correlated with an advanced chemical age, and also find that TMC1-1C does not appear to be chemically evolved. These results are consistent with our conclusion that the core is probably stable.

CB23: Our analysis shows that the $24\ \mu\text{m}$ shadow mass exceeds the Jeans mass by $\sim 25\%$, indicating that this core is only marginally unstable, if only thermal support is considered. The measured N_2H^+ line widths (see below) are narrow and indicate that the turbulent contribution to the support is only of order $\sim 30\%$ (Hotzel et al. 2002). A magnetic field of $\sim 120\ \mu\text{G}$ would be sufficient to support the $24\ \mu\text{m}$ mass and to halt collapse (Stahler & Palla 2005). A magnetic field of this level is on the high side of the range of field strengths measured for other cores (Bergin & Tafalla 2007), but remains plausible. Park et al. (2004) observe ^{12}CO and ^{13}CO emission; the line profiles appear Gaussian. Lee et al. (2004) observe CS (3–2) and DCO^+ (2–1); Lee et al. (1999) observe CS (2–1) and N_2H^+ (1–0). A blue asymmetry is observed in CS (2–1); a small amount of a blue asymmetry is seen in CS (3–2) and DCO^+ (2–1) although it falls below the Lee et al. (2004) threshold to be classified as a collapse candidate. Crapsi et al. (2005) measure the N_2H^+ (1–0) and N_2D^+ (2–1) line widths to be 0.17 and 0.23 km s^{-1} , respectively but do not classify this source as chemically or kinematically evolved.

⁸ The ^{13}CO emission sometimes appears to be bright along an edge of the shadow region (seen most clearly in L1552 and CB44) and in one case we clearly observe a deficit of emission in the region coincident with the shadow (L1544). These characteristics are likely caused by the freeze-out of CO on to dust grains, as well as by a non-uniform density and temperature structure in the cores.

Sohn et al. (2007) observe an infall asymmetry in the HCN (1–0) line profiles of at least 2 of the 3 hyper-fine components, and possibly in all three. We note that the Crapsi et al. (2005) and the Sohn et al. (2007) observations were taken at locations separated by $\sim 60''$, however, both locations are well within the shadow feature. Taken with our results, these observations indicate that this core is approaching collapse.

CB26: Our analysis indicates that this core has a mass that exceeds the Jeans criterion by a factor of ~ 3 . The field required to support the mass of CB26 is of order $200 \mu\text{G}$, much larger than the upper limit of $74 \mu\text{G}$ set by Henning et al. (2001) in a nearby region of CB26. The HCN (1-0) line widths of $\sim 0.6\text{--}0.9 \text{ km s}^{-1}$ measured by Turner et al. (1997) indicate that the turbulent support is of order ~ 2 to 4 times the thermal support; however, Turner et al. (1997) do not show their HCN measurement and our CO spectra show 2 velocity components, which could broaden the line widths (see Figure 24). We note that Turner et al. (1997) do not list the coordinates of these observations and we assume they are the same as those listed in Clemens & Barvainis (1988), which are about $1'$ from the center of the shadow. Without higher density tracer line profiles from which to infer the velocity field of the material, we consider it likely that CB26 is near collapse. The young T-Tauri star associated with this source has received far more attention than the nearby starless core. This YSO has been studied in detail (e.g., Launhardt et al. 1998; Henning et al. 2001; Stecklum et al. 2004; Launhardt et al. 2009; Sauter et al. 2009). It lies approximately $3.5'$ to the south-west of the shadow center, and can be seen in Figure 3 as the brightest $24 \mu\text{m}$ source. Although it is not clear what evolutionary, chemical, or other, relationship the shadow and the YSO might share, it is interesting that Henning et al. (2001) measure relatively well-ordered submillimeter dust polarization in a region $\sim 40''$ on a side towards the young star, perhaps indicating that the magnetic field in the larger region, and therefore in the shadow, might also be well behaved. The polarization vectors point roughly north-south, indicating that the magnetic field is oriented in the east-west direction, the same direction as the longer axis of the entire CB26 region.

CB27: Our analysis indicates that this source is stable, if supported only by thermal pressure. With an additional plausible level of turbulent and magnetic support, the core remains stable. This conclusion is supported by the molecular line observations, which show no evidence of asymmetry. Lee et al. (2004) measure CS (3–2) and DCO^+ (2–1) line profiles that are indistinguishable from Gaussian. Park et al. (2004) observe ^{12}CO and ^{13}CO Gaussian profiles as well. Sohn et al. (2007) observe this source to have a red asymmetry in all three HCN (1-0) line profiles. Gupta et al. (2009) detect C_6H^- emission with a line width of $\sim 0.15 \text{ km s}^{-1}$; Roberts & Millar (2007) detect N_2H^+ and N_2D^+ emission whose line profiles appear symmetric.

L1544: We find that our $24 \mu\text{m}$ mass is lower than the Jeans criterion for collapse; however, the $70 \mu\text{m}$ image indicates that this mass estimate is a *lower limit*. As can be seen in Figure 5, in the $70 \mu\text{m}$ image there is a hint of a dark region at the location of the $24 \mu\text{m}$ shadow. The quality of the $70 \mu\text{m}$ image does

not allow for a robust analysis; however, Stutz et al. (2009) show that in the case of starless core L429, the $24 \mu\text{m}$ shadow mass is underestimated compared to the $70 \mu\text{m}$ shadow by a factor ~ 5 . Taking this result, a plausible corrected $24 \mu\text{m}$ mass is $7 M_\odot$, a factor of ~ 2.5 larger than the Jeans mass, making the core much more likely to be approaching collapse. Many authors have observed this source (e.g., Lee et al. 1999; Bacmann et al. 2000; Shirley et al. 2000; Bacmann et al. 2002; Tafalla et al. 2002; Bacmann et al. 2003; Lee et al. 2003, 2004; Williams et al. 2006; Park et al. 2004; Caselli et al. 2008; Gupta et al. 2009); the consensus is that this starless core is very evolved and likely to be collapsing. Lee et al. (2004) observe a CS (3–2) profile with a double peak with a brighter blue peak, and a DCO^+ (2–1) profile with a blue asymmetry. Crapsi et al. (2005) measure the N_2H^+ (2-1) and N_2D^+ (2-1) line widths to be 0.32 and 0.29 km s^{-1} , respectively; the N_2H^+ (3-2) and N_2D^+ (3-2) were 0.19 and 0.34 km s^{-1} , respectively. They also find that this core has a large $\text{N}_2\text{D}^+/\text{N}_2\text{H}^+$ ratio equal to 0.23 and classify it as a highly evolved core, based on various observational chemical evolutionary probes. Williams et al. (2006) compare the N_2H^+ (1-0) emission from L1544 and L694-2 and conclude that both cores will form stars in $\sim 10^4 \text{ yr}$. Sohn et al. (2007) measure all three HCN (1-0) components to have two very strong peaks, all with the blue peak higher than the red peak. Bacmann et al. (2002) and Bacmann et al. (2003) find high degrees of CO depletion and a large deuterium abundance; Caselli et al. (2008) measure a large amount of ortho- H_2D^+ ($1_{1,0}\text{--}1_{1,1}$) emission, one of the highest in their sample, and conclude that emission from this species is correlated with CO depletion, deuterium fractionation, and an advanced chemical evolutionary stage. These results are consistent with our conclusion that this core is likely to be approaching collapse.

L1552: In this case, our analysis shows that the $24 \mu\text{m}$ shadow mass exceeds the Jeans mass by a wide margin, a factor of ~ 8 . This source also shows a clear detection of a $70 \mu\text{m}$ shadow; applying a correction of a factor of 5 to the $24 \mu\text{m}$ mass (see L1544 discussion and Stutz et al. 2009) makes this core very unstable. Lee et al. (2004) measure a blue asymmetry in both CS (3–2) and DCO^+ (2–1). The Sohn et al. (2007) HCN (1-0) profiles show a mild blue asymmetry in the line profiles and report an N_2H^+ narrow line width of 0.22 km s^{-1} , indicating that turbulent support is negligible. These line measurements are consistent with our conclusion that this core is near collapse.

CB42: Our analysis indicates that this source is very stable against collapse, with a Jeans mass that exceeds the shadow mass by a factor ~ 10 . Turner et al. (1997) measure an HCN line width of $\sim 0.82 \text{ km s}^{-1}$.

CB44: Our analysis indicates that this core has a mass that exceeds the Jeans criterion by a factor of ~ 12 . Molecular line observations of this source are sparse; however, Launhardt et al. (1998) measure a CS (2-1) line width of 1.5 km s^{-1} , with a profile showing some indication that it may have a red asymmetry. Observations of other (high density) tracers are needed. The magnetic field required to support the $24 \mu\text{m}$ shadow mass is of order $190 \mu\text{G}$, large compared to observations of other cores (Bergin & Tafalla 2007). Based on this evidence and without line observations of higher density tracers

we consider it likely that CB44 is approaching collapse.

L492: Our mass measurement indicates that this core may be unstable to collapse. Although the 24 μm mass only marginally exceeds the Jeans mass, by $\sim 15\%$, this source has a 70 μm shadow, which, as discussed above, indicates that the 24 μm mass is a lower limit (Stutz et al. 2009). Kauffmann et al. (2008) report a 1.2 mm dust mass of $18.35 \pm 0.17 M_{\odot}$, in reasonable agreement with our CO-measured mass of $23.6 M_{\odot}$, accounting for our larger CO aperture ($4'$). At both 8 μm and 24 μm we observe two sub-components of this core, oriented in the east-west direction; this structure is not evident in the Kauffmann et al. (2008) MAMBO maps. Crapsi et al. (2005) measure the $\text{N}_2\text{H}^+(2-1)$ and $\text{N}_2\text{D}^+(2-1)$ line widths to be 0.26 and 0.22 km s^{-1} , respectively, at a position centered on the western sub-clump. The narrow line widths indicate that turbulence does not play a significant role in the support of this core. They classify this source as marginally evolved because it exhibits only 3 out of the 8 evolutionary probes that they consider. Lee et al. (2004) measure a CS (3-2) with a blue asymmetry, $\text{DCO}^+(2-1)$ profile with a blue asymmetry and possible self absorption; they classify this source as an infall candidate. Sohn et al. (2007) measure all three HCN (1-0) components to have two strong peaks, all with the blue peak higher than the red peak, and consider this source to be an infall candidate. These results are consistent with our conclusion that this core is likely to be approaching collapse.

CB130: In the case of CB130, the 24 μm shadow mass is only marginally unstable. A plausible level of turbulent and/or magnetic support would halt collapse; for example, a magnetic field of $\sim 70 \mu\text{G}$ will suffice to halt collapse. There are no molecular line observations at the location of the shadow. The source CB130-3, which lies $1.5'$ east of the shadow center, is the closest object and was studied by Park et al. (2004) and Lee et al. (2004). Inspection of the DSS red plate reveals what appears to be a cusp, or knot, of material at the CB130-3 position. However, our 24 μm maps indicate that a denser and compact region of the CB130 complex is revealed by the 24 μm shadow which is completely enshrouded at near-IR and shorter wavelengths (see Figure 10). At the CB130-3 position Lee et al. (2004) measure a CS (3-2) line profile with a red asymmetry. Without further molecular line observations, we conclude that this source is probably stable.

CB180: Our analysis indicates that this source is unstable, with a 24 μm shadow mass that exceeds the Jeans mass by a factor of ~ 2.6 . Caselli et al. (2002) measure an N_2H^+ line width of 0.9 km s^{-1} but do not show the spectrum of this object; this width indicates that the contribution of turbulence is about 4 times that of the thermal support (Hotzel et al. 2002). Given the 24 μm shadow mass, a magnetic field of order $\sim 70 \mu\text{G}$ would suffice to halt collapse. Based on these pieces of evidence, and without kinematical information from detailed line profiles, we consider it likely that CB180 is close to collapse.

L694-2: Our 24 μm mass indicates that this core is stable; however, as with L1544, L1552, and L492, this source has a 70 μm shadow. Correcting our 24 μm mass by a factor 5, as discussed above, yields a core mass that exceeds the Jeans mass by a factor of ~ 4 . Like L1544, this source has been studied in some detail (e.g., Lee et al.

1999; Harvey et al. 2003a,b; Lee et al. 2004; Crapsi et al. 2005; Williams et al. 2006; Lee et al. 2007; Sohn et al. 2007; Caselli et al. 2008). Crapsi et al. (2005) measure the $\text{N}_2\text{H}^+(2-1)$ and $\text{N}_2\text{D}^+(2-1)$ line widths to be 0.27 and 0.24 km s^{-1} , respectively; the $\text{N}_2\text{H}^+(3-2)$ and $\text{N}_2\text{D}^+(3-2)$ were 0.31 and 0.24 km s^{-1} , respectively. They also find that this core has a large $\text{N}_2\text{D}^+/\text{N}_2\text{H}^+$ ratio equal to 0.26. Similar to L1544, this core is classified by Crapsi et al. (2005) as highly evolved, both chemically and kinematically. Sohn et al. (2007) measure HCO (1-0) double-peaked line profiles with a blue asymmetry. Caselli et al. (2008) measure a large amount of ortho- $\text{H}_2\text{D}^+(1_{1,0}-1_{1,1})$ emission, one of the highest in their sample, along with L1544 (and L429). The line widths indicate that the turbulent support is negligible, contributing of order $\sim 0.4\times$ the thermal support. These results are consistent with our conclusion that this core is approaching collapse.

Here we summarize results from two previous studies of cores CB190 (Stutz et al. 2007) and L429 (Stutz et al. 2009) which use similar techniques applied to 24 μm and 70 μm shadows, respectively:

CB190: Stutz et al. (2007) carry out a detailed study of this core. The 24 μm shadows analysis indicates that the mass of the core is twice the Jeans mass; however, the magnetic field required to support the core material is about 90 μG , a plausible field strength for starless cores. If the magnetic field is in fact present in CB190 it will leak out of the core in ~ 3 Myr, an ambipolar diffusion time-scale (Stahler & Palla 2005). Turbulent pressure does not provide sufficient support against collapse. Millimeter line emission from various species is too faint to constrain the kinematics in the core. Without more line profile information, we conclude that CB190 is near collapse.

L429: Stutz et al. (2009) study the 70 μm shadow cast by this core and conclude that a plausible level of magnetic support will not halt collapse. Additionally, the molecular line widths are narrow, indicating that the turbulent support is of order the thermal support in this core. Stutz et al. (2009) conclude that L429 is in a near collapse state. Lee et al. (2004) observe a blue asymmetry in the CS (3-2) line, while Crapsi et al. (2005) and Lee et al. (1999) measure symmetrical double peaked $\text{N}_2\text{H}^+(1-0)$ and CS (2-1) lines, respectively. Sohn et al. (2007) measure HCN (1-0) double peaked lines but note that this source is one of two out of 85 cores in their study with anomalous hyperfine line ratios. More high-resolution line observations are needed to clarify these results. Caselli et al. (2008) measure a large amount of ortho- $\text{H}_2\text{D}^+(1_{1,0}-1_{1,1})$ emission for this source, and find that this emission is correlated with a large degree of central concentration, and a large amount of CO depletion and deuteration, indicating that this source is evolved. Taken together, these pieces of evidence indicate L429 is close to collapse.

In this paper we emphasize how the 24 μm shadow observations can reveal structure not evident in previous studies. We highlight the 24 μm observations of CB130 and L492. In the case of L492, we observe what appear to be 2 sub-clumps in the shadow feature (Figure 9), oriented in a roughly east-west direction separated by about $40''$, reported here for the first time. Molecular line observations are centered on the western component (e.g.,

Crapsi et al. 2005) and indicate that this core is likely to be collapsing. The two components may be an example of core fragmentation; high spatial resolution observations of this core should be able to confirm if both sub-clumps are collapsing, and to measure the relative radial velocity between them. In the case of CB130, we have discovered a 24 μm shadow which is $\sim 1'.5$ west of the region previously selected for millimeter line studies (e.g., Lee et al. 2004; Park et al. 2004); further observations taken at the location of the 24 μm shadow will confirm if this core is near collapse.

In the top panel of Figure 28 we compare the 24 μm shadow masses (M_{24}^{core} in Table 4) to the CO-derived core masses ($M_{\text{CO}}^{\text{core}}$ in Table 4). In all cases, $F_{\text{core}} = M_{24}^{\text{core}}/M_{\text{CO}}^{\text{core}} \geq 1.0$; this discrepancy is likely due to the effect of freeze-out of CO in dense regions (e.g., Bacmann et al. 2002; Tafalla et al. 2002); the effect will be stronger that illustrated for cores with 70 μm shadows (L1544, L1552, L492, and L694-2, see above discussion) because the 24 μm mass is likely to be underestimated. In the lower panel of Figure 28 we show the 24 μm masses as a function of the total molecular CO derived masses (integrated over a 4' radius). Cores with 70 μm shadows are marked with grey arrows indicating a plausible mass correction of a factor of 5 (Stutz et al. 2009). We tentatively detect a rough trend in core mass with increasing envelope mass. We caution that this trend may be driven by distance uncertainties, small sample size, and incomplete mass census. Observations from upcoming facilities, e.g., SCUBA2, which can image the sub-millimeter dust continuum emission, and *Herschel*, which can image the 70 μm shadows with a high degree of spatial resolution ($\sim 6''$) will provide further constraints on the evolution of starless cores.

5. CONCLUSIONS

We study the 8 μm , 24 μm , and 70 μm shadows cast by a sample of 14 starless cores. We derive 24 μm core

masses and sizes; we apply a Jeans mass criterion, and attempt to account for turbulent and magnetic support in the cores, in order to assess the collapse state of each core. We caution that distance uncertainties can have a large effect on our Jeans mass analysis. In addition, we have obtained ^{12}CO (2-1) and ^{13}CO (2-1) OTF maps of the cores; the molecular core masses we derive are always less than the 24 μm masses. This discrepancy is likely caused by freezeout onto dust grains. From this work we conclude that:

1. 70% (10/14) of cores selected to have prominent 24 μm shadows seem to be approaching collapse, indicating that this criterion selects dense, evolved cores.
2. 50% (5/10) of cores that are classified as approaching collapse have indications of 70 μm shadows; the 70 μm data quality does not allow for a rigorous analysis of these shadows.
3. All cores with indications of 70 μm shadows have millimeter line profiles showing blue asymmetries, indicating that these long-wavelength shadow features are produced by very evolved cores. These cores are all likely to be close to collapse.
4. Shadows at 24 μm and especially at 70 μm appear to be effective indicators of cores that are approaching collapse.

A. M. S. thanks Juna Kollmeier for her early input and stimulating discussions throughout the course of this work. The authors thank Craig A. Kulesa for assistance with the molecular mass models and Chris Walker for helpful comments. We also thank the anonymous referee for their helpful comments. Support for this work was provided through NASA contracts issued by Caltech/JPL to the University of Arizona (1255094). This work was also supported by the National Science Foundation grant AST-0708131 to The University of Arizona. MK was supported by the KRF-2007-612-C00050 grant.

REFERENCES

- Alves, J. F., Lada, C. J., & Lada, E. A. 2001, *Nature*, 409, 159
- Alves, F. O., Franco, G. A. P., & Girart, J. M. 2008, *A&A*, 486, L13
- Arquilla, R., & Goldsmith, P. F. 1986, *ApJ*, 303, 356
- Bacmann, A., André, P., Puget, J.-L., Abergel, A., Bontemps, S., & Ward-Thompson, D. 2000, *A&A*, 361, 555
- Bacmann, A., Lefloch, B., Ceccarelli, C., Castets, A., Steinacker, J., & Loinard, L. 2002, *A&A*, 389, L6
- Bacmann, A., Lefloch, B., Ceccarelli, C., Steinacker, J., Castets, A., & Loinard, L. 2003, *ApJ*, 585, L55
- Ballesteros-Paredes, J., Klessen, R. S., & Vázquez-Semadeni, E. 2003, *ApJ*, 592, 188
- Bergin, E. A., & Tafalla, M. 2007, *ARA&A*, 45, 339
- Bok, B. J., & McCarthy, C. C. 1974, *AJ*, 79, 42
- Burkert, A., & Bodenheimer, P. 2000, *ApJ*, 543, 822
- Burkert, A., & Hartmann, L. 2004, *ApJ*, 616, 288
- Butler, M. J., & Tan, J. C. 2009, *ApJ*, 696, 484
- Caselli, P., Walmsley, C. M., Tafalla, M., Dore, L., & Myers, P. C. 1999, *ApJ*, 523, L165
- Caselli, P., Benson, P. J., Myers, P. C., & Tafalla, M. 2002, *ApJ*, 572, 238
- Caselli, P., Vastel, C., Ceccarelli, C., van der Tak, F. F. S., Crapsi, A., & Bacmann, A. 2008, *A&A*, 492, 703
- Chapman, N. L., Mundy, L. G., Lai, S.-P., & Evans, N. J. 2009, *ApJ*, 690, 496
- Chapman, N. L., & Mundy, L. G. 2009, arXiv:0905.0655
- Clemens, D. P., & Barvainis, R. 1988, *ApJS*, 68, 257
- Crapsi, A., Caselli, P., Walmsley, C. M., Myers, P. C., Tafalla, M., Lee, C. W., & Bourke, T. L. 2005, *ApJ*, 619, 379
- de Wit, W. J., Testi, L., Palla, F., & Zinnecker, H. 2005, *A&A*, 437, 247
- Draine, B. T. 2003, *ARA&A*, 41, 241
- Evans, N. J., Rawlings, J. M. C., Shirley, Y. L., & Mundy, L. G. 2001, *ApJ*, 557, 193
- Fallscheer, C., Beuther, H., Zhang, Q., Keto, E., & Sridharan, T. K. 2009, arXiv:0907.2232
- Flaherty, K. M., Pipher, J. L., Megeath, S. T., Winston, E. M., Gutermuth, R. A., Muzerolle, J., Allen, L. E., & Fazio, G. G. 2007, *ApJ*, 663, 1069
- Foster, J. B., & Goodman, A. A. 2006, *ApJ*, 636, L105
- Gregersen, E. M., Evans, N. J., II, Zhou, S., & Choi, M. 1997, *ApJ*, 484, 256
- Gregersen, E. M., & Evans, N. J., II 2000, *ApJ*, 538, 260
- Gordon, K. D., et al. 2005, *PASP*, 117, 503
- Gupta, H., Gottlieb, C. A., McCarthy, M. C., & Thaddeus, P. 2009, *ApJ*, 691, 1494
- Gutermuth, R. A., et al. 2008, *ApJ*, 674, 336
- Harvey, D. W. A., Wilner, D. J., Lada, C. J., Myers, P. C., & Alves, J. F. 2003a, *ApJ*, 598, 1112
- Harvey, D. W. A., Wilner, D. J., Myers, P. C., & Tafalla, M. 2003b, *ApJ*, 597, 424
- Hayashi, C. 1966, *ARA&A*, 4, 171
- Heitsch, F., Hartmann, L. W., Slyz, A. D., Devriendt, J. E. G., & Burkert, A. 2008, *ApJ*, 674, 316
- Henning, T., Wolf, S., Launhardt, R., & Waters, R. 2001, *ApJ*, 561, 871
- Hilton, J., & Lahulla, J. F. 1995, *A&AS*, 113, 325
- Hotzel, S., Harju, J., & Juvela, M. 2002, *A&A*, 395, L5

- Juvela, M., Pelkonen, V.-M., Padoan, P., & Mattila, K. 2008, *A&A*, 480, 445
- Kandori, R., et al. 2005, *AJ*, 130, 2166
- Kang, M., Biegging, J. H., Kulesa, C. A., & Lee, Y. 2009, *ApJ*, 701, 454
- Kauffmann, J., Bertoldi, F., Bourke, T. L., Evans, N. J., II, & Lee, C. W. 2008, *A&A*, 487, 993
- Kawamura, A., Kun, M., Onishi, T., Vavrek, R., Domsa, I., Mizuno, A., & Fukui, Y. 2001, *PASJ*, 53, 1097
- Kenyon, S. J., Dobrzycka, D., & Hartmann, L. 1994, *AJ*, 108, 1872
- Kulesa, C. A., Hungerford, A. L., Walker, C. K., Zhang, X., & Lane, A. P. 2005, *ApJ*, 625, 194
- Kutner, M. L., & Ulich, B. L. 1981, *ApJ*, 250, 341
- Lada, C. J., & Lada, E. A. 2003, *ARA&A*, 41, 57
- Lada, C. J., Muench, A. A., Rathborne, J., Alves, J. F., & Lombardi, M. 2008, *ApJ*, 672, 410
- Lallement, R., Welsh, B. Y., Vergely, J. L., Crifo, F., & Sfeir, D. 2003, *A&A*, 411, 447
- Launhardt, R., Evans, N. J., II, Wang, Y., Clemens, D. P., Henning, T., & Yun, J. L. 1998, *ApJS*, 119, 59
- Launhardt, R., et al. 2009, *A&A*, 494, 147
- Lee, C. W., Myers, P. C., & Tafalla, M. 1999, *ApJ*, 526, 788
- Lee, J.-E., Evans, N. J., II, Shirley, Y. L., & Tatematsu, K. 2003, *ApJ*, 583, 789
- Lee, C. W., Myers, P. C., & Plume, R. 2004, *ApJS*, 153, 523
- Lee, S. H., Park, Y.-S., Sohn, J., Lee, C. W., & Lee, H. M. 2007, *ApJ*, 660, 1326
- Lee, M.-Y., et al. 2009, arXiv:0908.2275
- Lehtinen, K., & Mattila, K. 1996, *A&A*, 309, 570
- Lemme, C., Wilson, T. L., Tieftrunk, A. R., & Henkel, C. 1996, *A&A*, 312, 585
- Mardones, D., Myers, P. C., Tafalla, M., Wilner, D. J., Bachiller, R., & Garay, G. 1997, *ApJ*, 489, 719
- Menten, K. M., Serabyn, E., Guesten, R., & Wilson, T. L. 1987, *A&A*, 177, L57
- Mundy, L. G., Wootten, H. A., & Wilking, B. A. 1990, *ApJ*, 352, 159
- Myers, P. C. 2005, *ApJ*, 623, 280
- Nakajima, Y., Kandori, R., Tamura, M., Nagata, T., Sato, S., & Sugitani, K. 2008, *PASJ*, 60, 731
- Narayanan, G., Walker, C. K., & Buckley, H. D. 1998, *ApJ*, 496, 292
- Ossenkopf, V., & Henning, T. 1994, *A&A*, 291, 943
- Padoan, P., Juvela, M., & Pelkonen, V.-M. 2006, *ApJ*, 636, L101
- Park, Y.-S., Lee, C. W., & Myers, P. C. 2004, *ApJS*, 152, 81
- Perault, M., et al. 1996, *A&A*, 315, L165
- Peretto, N., & Fuller, G. A. 2009, arXiv:0906.3493
- Povich, M. S., et al. 2009, *ApJ*, 696, 1278
- Roberts, H., & Millar, T. J. 2007, *A&A*, 471, 849
- Sault R.J., Teuben P.J., Wright M.C.H., 1995, in *Astronomical Data Analysis Software and Systems IV*, ed. R. Shaw, H.E. Payne, J.J.E. Hayes, ASP Conf. Ser., 77, 433-436
- Sauter, J., et al. 2009, arXiv:0907.1074
- Shirley, Y. L., Evans, N. J., II, Rawlings, J. M. C., & Gregersen, E. M. 2000, *ApJS*, 131, 249
- Shirley, Y. L., Nordhaus, M. K., Grcevich, J. M., Evans, N. J., Rawlings, J. M. C., & Tatematsu, K. 2005, *ApJ*, 632
- Shu, F. H., Adams, F. C., & Lizano, S. 1987, *ARA&A*, 25, 23
- Sohn, J., Lee, C. W., Park, Y.-S., Lee, H. M., Myers, P. C., & Lee, Y. 2007, *ApJ*, 664, 928
- Stahler, S. W., & Palla, F. 2005, *The Formation of Stars*, by Steven W. Stahler, Francesco Palla, pp. 865. ISBN 3-527-40559-3. Wiley-VCH, January 2005.
- Straizys, V., Černis, K., & Bartašiūtė, S. 2003, *A&A*, 405, 585
- Stecklum, B., Launhardt, R., Fischer, O., Henden, A., Leinert, C., & Meusinger, H. 2004, *ApJ*, 617, 418
- Stutz, A. M., et al. 2007, *ApJ*, 665, 466
- Stutz, A. M., Papovich, C., & Eisenstein, D. J. 2008a, *ApJ*, 677, 828
- Stutz, A. M., et al. 2008b, *ApJ*, 687, 389
- Stutz, A. M., Bourke, T. L., Rieke, G. H., Biegging, J. H., Misselt, K. A., Myers, P. C., & Shirley, Y. L. 2009, *ApJ*, 690, L35
- Tafalla, M., Myers, P. C., Caselli, P., Walmsley, C. M., & Comito, C. 2002, *ApJ*, 569, 815
- Tomita, Y., Saito, T., & Ohtani, H. 1979, *PASJ*, 31, 407
- Torres, R. M., Loinard, L., Mioduszewski, A. J., & Rodriguez, L. F. 2009, arXiv:0903.5338
- Turner, B. E., Pirogov, L., & Minh, Y. C. 1997, *ApJ*, 483, 235
- van Dishoeck, E. F., & Black, J. H. 1988, *ApJ*, 334, 771
- Walker, C. K., Lada, C. J., Young, E. T., Maloney, P. R., & Wilking, B. A. 1986, *ApJ*, 309, L47
- Walker, C. K., Lada, C. J., Young, E. T., & Margulis, M. 1988, *ApJ*, 332, 335
- Williams, J. P., Lee, C. W., & Myers, P. C. 2006, *ApJ*, 636, 952

TABLE 1
Spitzer IRAC AND MIPS DATA PARAMETERS

Source	Other names	R.A. h m s	Decl. ° ' "	l °	b °	MIPS AOR ^a	IRAC AOR ^a
(1)	(2)	(3)	(4)	(5)	(6)	(7)	(8)
TMC1-1C	B220	04 41 51.4	+25 50 13	174.3	-13.3	18155008	5085952
CB23	L1507	04 43 27.9	+29 42 26	171.5	-10.6	12026368	4914944
CB26	L1439	04 59 59.8	+52 03 29	156.1	+5.9	12020480	4916224
CB27	L1512	05 04 05.3	+32 46 03	171.8	-5.2	12021248	4916736
L1544	...	05 04 17.4	+25 08 23	178.0	-9.8	18155776	14610688
L1552	...	05 17 38.2	+26 02 53	179.0	-6.8	18156288	4917760
CB42	...	06 02 47.5	+16 43 00	192.5	-2.8	12024064	...
CB44	B227,L1570	06 07 31.0	+19 31 00	190.6	-0.4	12022272	4919296
L492	CB128	18 15 49.1	-03 43 05	25.5	+6.1	18159360	14603264
CB130	L507	18 16 14.3	-02 30 16	26.7	+6.6	18159616	5146368
CB180	B133,L531	19 06 15.1	-06 55 25	28.4	-6.4	12023808	4925696
L694-2	B143,CB200	19 41 07.4	+10 58 59	48.4	-5.8	18160128	14604288

NOTE. — Coordinates indicate the reference pixel coordinate for each listed observation.
^a AOR = Astronomical Observation Request

TABLE 2
HHT OTF MAPPING PARAMETERS

Core	R.A. h m s	Decl. ° ' "	Obs. Date	Size ' × '	Line	T_{sys} ^a K	RMS ^b K - T_A^*	Vel. ^c km s ⁻¹
(1)	(2)	(3)	(4)	(5)	(6)	(7)	(8)	(9)
TMC1	04 41 37.5	+26 02 34	2009 Feb 01	10 × 10	¹² CO (2-1)	203	0.15	2.0, 10.0
					¹³ CO (2-1)	222	0.11	4.0, 7.0
CB23	04 43 19.1	+29 43 43	2008 Feb 07	13 × 13	¹² CO (2-1)	241	0.22	4.0, 11.0
					¹³ CO (2-1)	221	0.15	5.0, 8.0
CB26	05 00 19.9	+52 05 56	2009 Mar 02	14 × 12	¹² CO (2-1)	263	0.17	1.7, 7.5
					¹³ CO (2-1)	255	0.25	3.0, 7.0
CB27B	05 04 10.5	+32 43 00	2007 Jan 28	15 × 15	¹² CO (2-1)	218	0.24	6.0, 8.3
					¹³ CO (2-1)	231	0.25	6.0, 8.0
L1544	05 04 16.9	+25 11 50	2009 Feb 01	10 × 10	¹² CO (2-1)	201	0.12	7.0, 10.0
					¹³ CO (2-1)	220	0.10	6.0, 8.0
L1552-SH	05 17 38.6	+26 05 29	2009 Feb 02	10 × 10	¹² CO (2-1)	190	0.15	5.0, 10.0
					¹³ CO (2-1)	207	0.13	7.0, 9.0
CB42	06 02 34.2	+16 57 04	2008 Apr 16	10 × 10	¹² CO (2-1)	264	0.19	-2.0, 9.0
					¹³ CO (2-1)	249	0.18	1.0, 4.0
CB44	06 07 29.2	+19 27 33	2007 Jan 28	10 × 10	¹² CO (2-1)	193	0.24	-5.0, 3.0
					¹³ CO (2-1)	207	0.26	-2.0, 1.0
L492	18 15 49.2	-03 44 11	2009 Mar 01	10 × 7	¹² CO (2-1)	299	0.24	0.0, 10.0
					¹³ CO (2-1)	289	0.33	6.0, 9.0
CB130-1	18 15 59.8	-02 13 28	2009 Mar 01	12 × 12	¹² CO (2-1)	261	0.19	1.0, 11.0
					¹³ CO (2-1)	246	0.27	5.0, 9.0
CB180	19 06 14.8	-06 48 18	2008 Apr 18	10 × 7	¹² CO (2-1)	209	0.15	9.0, 14.0
					¹³ CO (2-1)	196	0.15	11.0, 13.0
L694-2	19 41 05.3	+10 54 54	2009 Mar 01	10 × 10	¹² CO (2-1)	297	0.22	7.0, 11.0
					¹³ CO (2-1)	295	0.18	8.5, 10.5

NOTE. — The beam size (FWHM) for the HHT at the observed frequencies is $\sim 32''$ FWHM; the velocity resolution for these observations is 0.34 km s⁻¹. Objects observed in 2008 and later were observed using the ALMA prototype mixer, see text for details.

^a Single side-band system temperature.

^b Final OTF map RMS per pixel per velocity channel.

^c Velocity range of CO emission.

TABLE 3
SHADOW PARAMETERS

Source	R.A. h m s	Decl. ° ' "	Dist. ^a pc	$f_{\text{DC},24}^b$ $\mu\text{Jy}/\text{arcsec}^2$	$f_{0,24}$ $\mu\text{Jy}/\text{arcsec}^2$	$f_{\text{DC},8}^c$ MJy/sr	$f_{0,8}$ MJy/sr
(1)	(2)	(3)	(4)	(5)	(6)	(7)	(8)
TMC1-1C	04 41 39.1	+26 00 19	140	1390.63	11.49	957.92	38.98
CB23	04 43 29.5	+29 39 11	140	-4.51	3.15	1578.37	1.96
CB26	05 00 12.6	+52 06 02	140	-5.60	2.56	1741.00	14.63
CB27	05 04 08.6	+32 43 23	140	-7.67	5.82	903.63	3.88
L1544	05 04 16.7	+25 10 42	140	1555.05	12.36	4294.04	66.20
L1552	05 17 38.8	+26 05 05	140	1530.99	2.20	1456.65	17.89
CB42	06 02 27.7	+16 56 59	200	-11.0	10.45
CB44	06 07 29.0	+19 27 42	400	-7.30	3.89	1089.62	28.00
L492	18 15 48.6	-03 45 44	225	1075.20	7.79	2402.96	26.16
CB130	18 16 11.1	-02 16 38	225	788.42	7.30	835.85	28.29
CB180	19 06 08.4	-06 52 56	400	-5.78	4.60	865.37	30.85
L694-2	19 41 04.1	+10 57 10	230	627.72	6.22	1511.84	45.87

NOTE. — The listed values of $f_{0,8}$ and $f_{0,24}$ are the f_{DC} -subtracted quantities. Coordinates indicate the approximate centers of the shadow features shown in Figures 1–12. We also note that $1 \mu\text{Jy}/\text{arcsec}^2 = 23.5 \text{ MJy}/\text{sr}$

^a A discussion of the adopted distances and associated references is included in § 3.2.

^b $f_{\text{DC},24}$ indicated the 0.5 percentile pixel value in the $24 \mu\text{m}$ image.

^c $f_{\text{DC},8}$ indicated the 0.1 percentile pixel value in the $8 \mu\text{m}$ image.

TABLE 4
CORE MASSES AND SIZES

Source	M_{24}^{core} M_{\odot}	$M_{\text{CO}}^{\text{core } a}$ M_{\odot}	$M_{\text{CO},4}^b$ M_{\odot}	$R_{\text{eff}}^{\text{core } c}$ arcmin	$R_{\text{eff}}^{\text{core } c}$ pc	$F^{\text{core } d}$	$M_{\text{J}}^{\text{core } e}$ M_{\odot}
(1)	(2)	(3)	(4)	(5)	(6)	(7)	(8)
TMC1-1C	1.6	0.9	7.1	1.4	0.06	1.8	2.7
CB23	2.5	0.7	4.9	1.3	0.05	3.8	2.0
CB26	5.0	0.8	5.0	1.4	0.06	6.0	1.6
CB27	2.1	0.8	5.6	1.4	0.06	2.5	2.4
L1544 ^g	1.4	0.8	6.4	1.4	0.06	1.7	2.8
L1552 ^g	8.7	0.8	6.8	1.3	0.05	10.6	1.1
CB42	0.3	0.3	2.9	1.2	0.04	1.0	3.0
CB44	35.0	7.0	46.2	1.4	0.16	5.0	2.8
L492 ^g	3.8	2.0	16.1	1.3	0.09	1.9	3.3
CB130	3.2	1.5	15.6	1.2	0.08	2.1	3.1
CB180	10.2	5.3	51.5	1.2	0.13	1.9	3.9
L694-2 ^g	2.6	1.7	16.3	1.2	0.08	1.6	3.6

^a CO mass integrated over $R_{\text{eff}}^{\text{core}}$, centered on the shadow coordinates.

^b CO mass integrated over an $4'$ -radius aperture, centered on the shadow coordinates.

^c Effective radius of the $24 \mu\text{m}$ shadow, see § 4.2.1.

^d Ratio of M_{24}^{core} over $M_{\text{CO}}^{\text{core}}$.

^e Jeans mass assuming all cores are at 10 K, using the M_{24}^{core} and $R_{\text{eff}}^{\text{core}}$ to calculate the mean density in each core.

^f Rotational velocity required to support a core mass of M_{24}^{core} for a core size of $R_{\text{eff}}^{\text{core}}$.

^g Although the quality of the $70 \mu\text{m}$ data does not allow for robust measurements, these cores show strong indications of having $70 \mu\text{m}$ shadows. The presence of a $70 \mu\text{m}$ shadow implies that the cores are optically thick at shorter wavelengths; hence M_{24}^{core} should be regarded as a lower limit.

TABLE 5
STABILITY ANALYSIS SUMMARY

Source	Near Collapse	M_{24}^{core}/M_j^{core}	70 μm Shadow	B^a μG	E_{turb}/E_{th}^b	V_{rot}^c km s^{-1}	Chem. Evol.
(1)	(2)	(3)	(4)	(5)	(6)	(7)	(8)
TMC1-1C	no	0.6	no	0	0	0.4	no
CB23	yes	1.3	no	123	0.3	0.6	no
CB26	yes	3.2	no	214	2	0.5	...
CB27	no	0.9	no	0	0	0.6	...
L1544	yes	>0.5	yes	>66	0.4	>0.4	yes
L1552	yes	>8.1	yes	>424	0.2	>0.2	...
CB42	no	0.1	no	0	0	1.0	...
CB44	yes	12.	no	188	11	0.3	...
L492	yes	>1.1	yes	>71	0.3	>0.8	yes
CB130	no	1.0	no	0	...	0.4	...
CB180	yes	2.6	no	81	4	0.4	...
L694-2	yes	>0.7	yes	>57	0.4	>0.4	yes
CB190	yes	2.5	no	78	>0.5	0.6	...
L429	yes	>1.0	yes	>194	1	>0.4	yes

NOTE. — See SS 4.3 for full discussion.

^a Magnetic field strength required to halt collapse.

^b Calculated from line widths collected from the literature, see § 4.3 for references.

^c Rotational velocity required for stability.

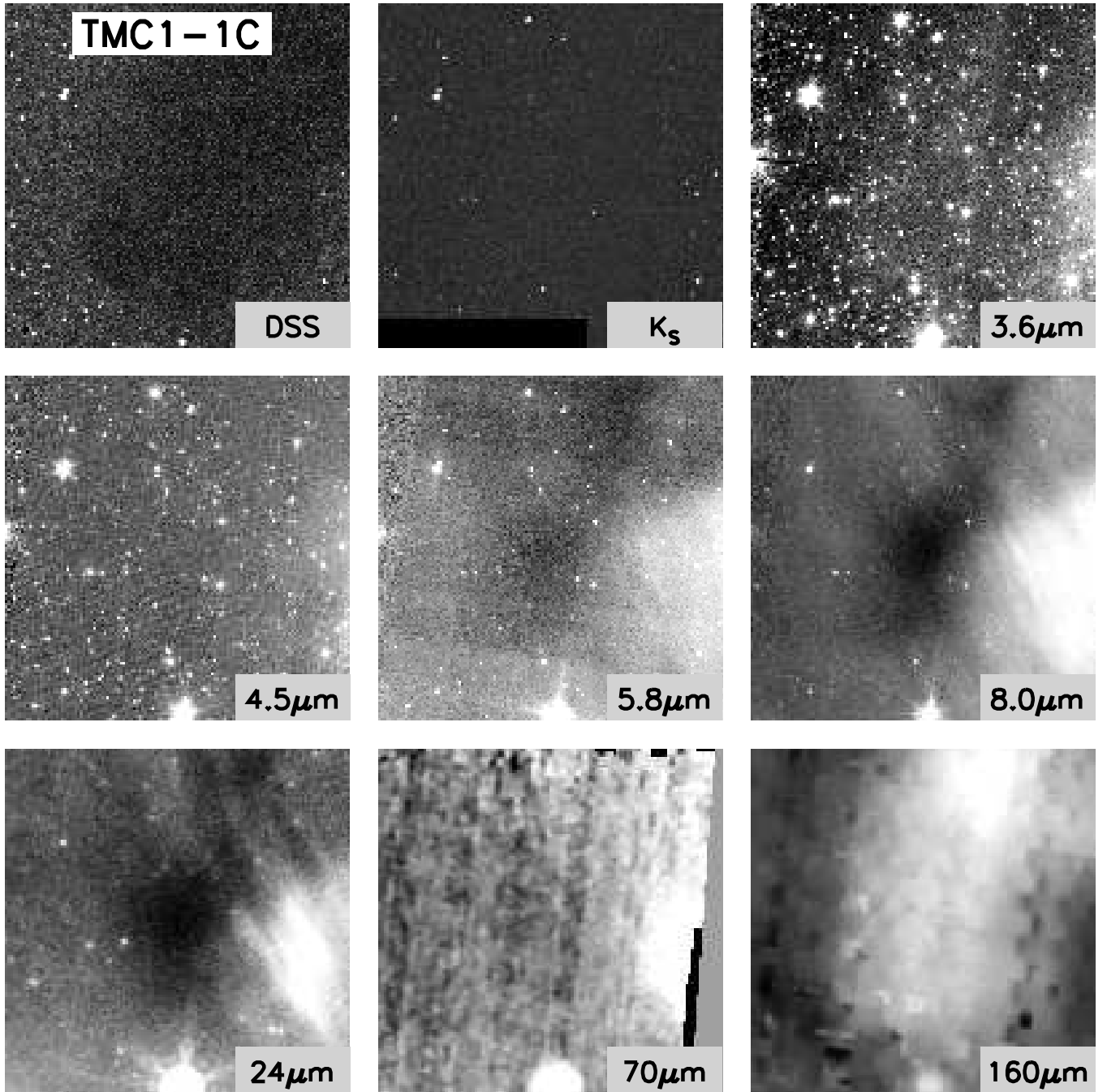


FIG. 1.— $8' \times 8'$ images at the indicated wavelengths, shown on a log scale. North is up, east is to the left. For full resolution figures contact stutz@mpia.de.

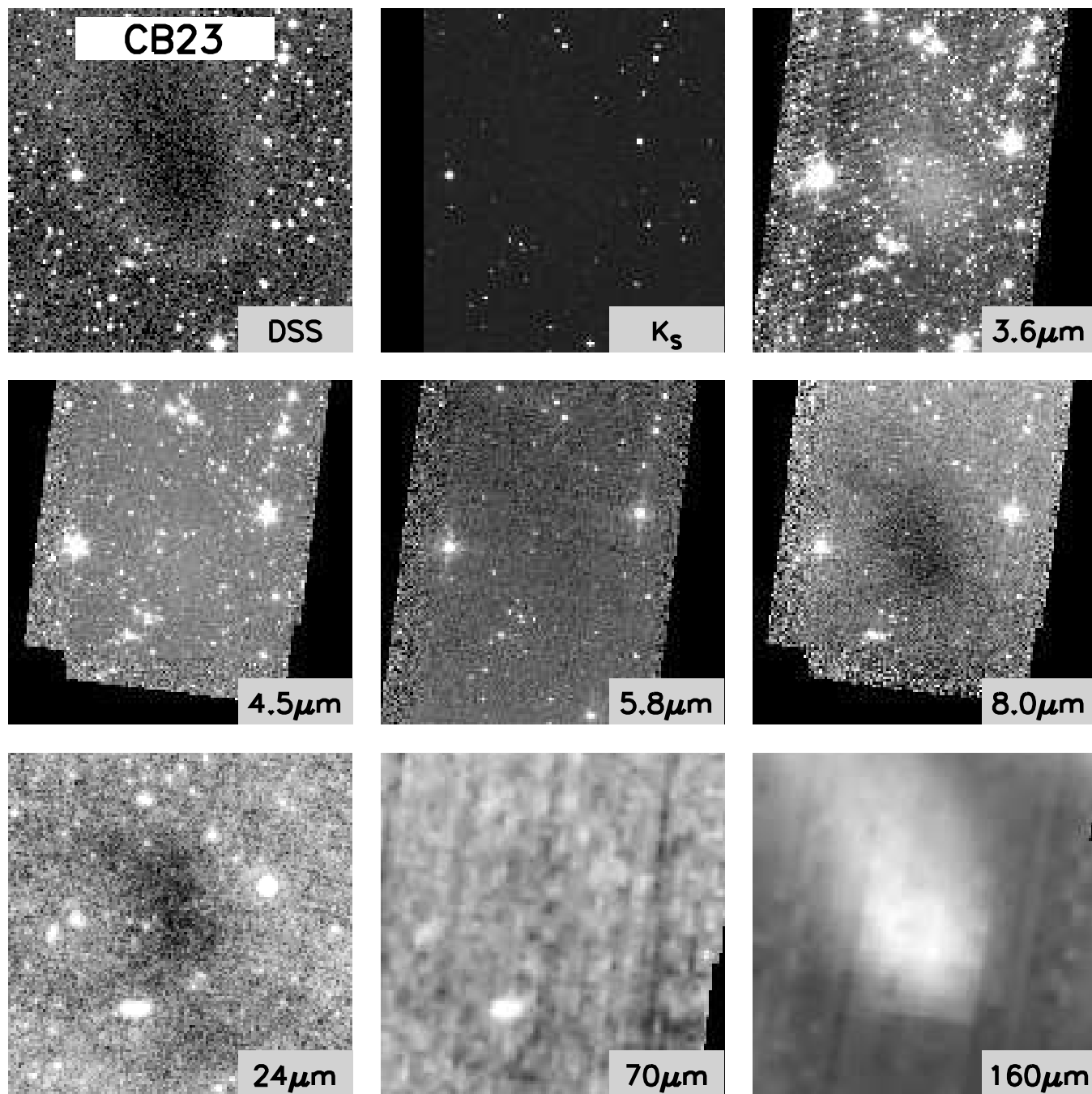


FIG. 2.— Same as Figure 1

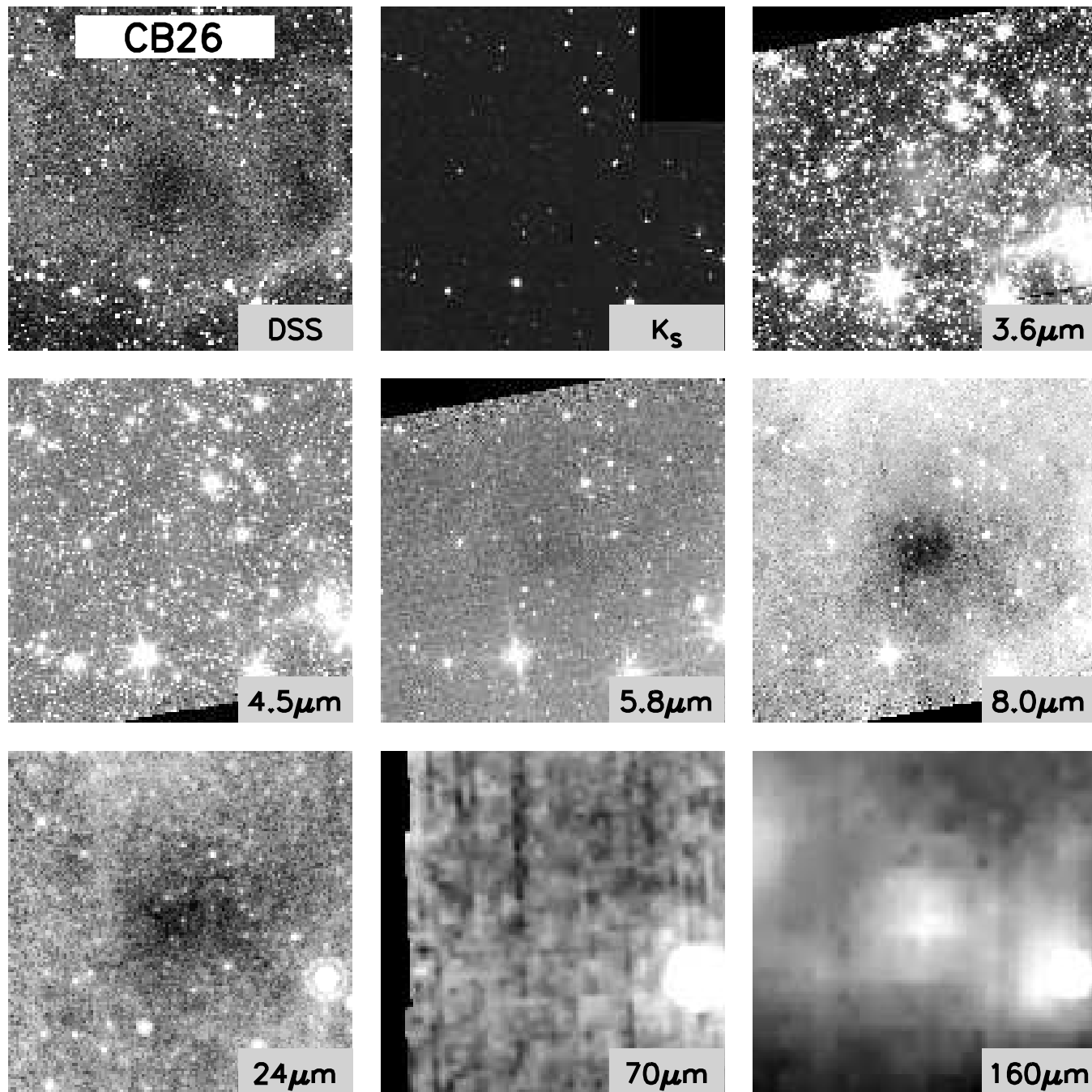


FIG. 3.— Same as Figure 1

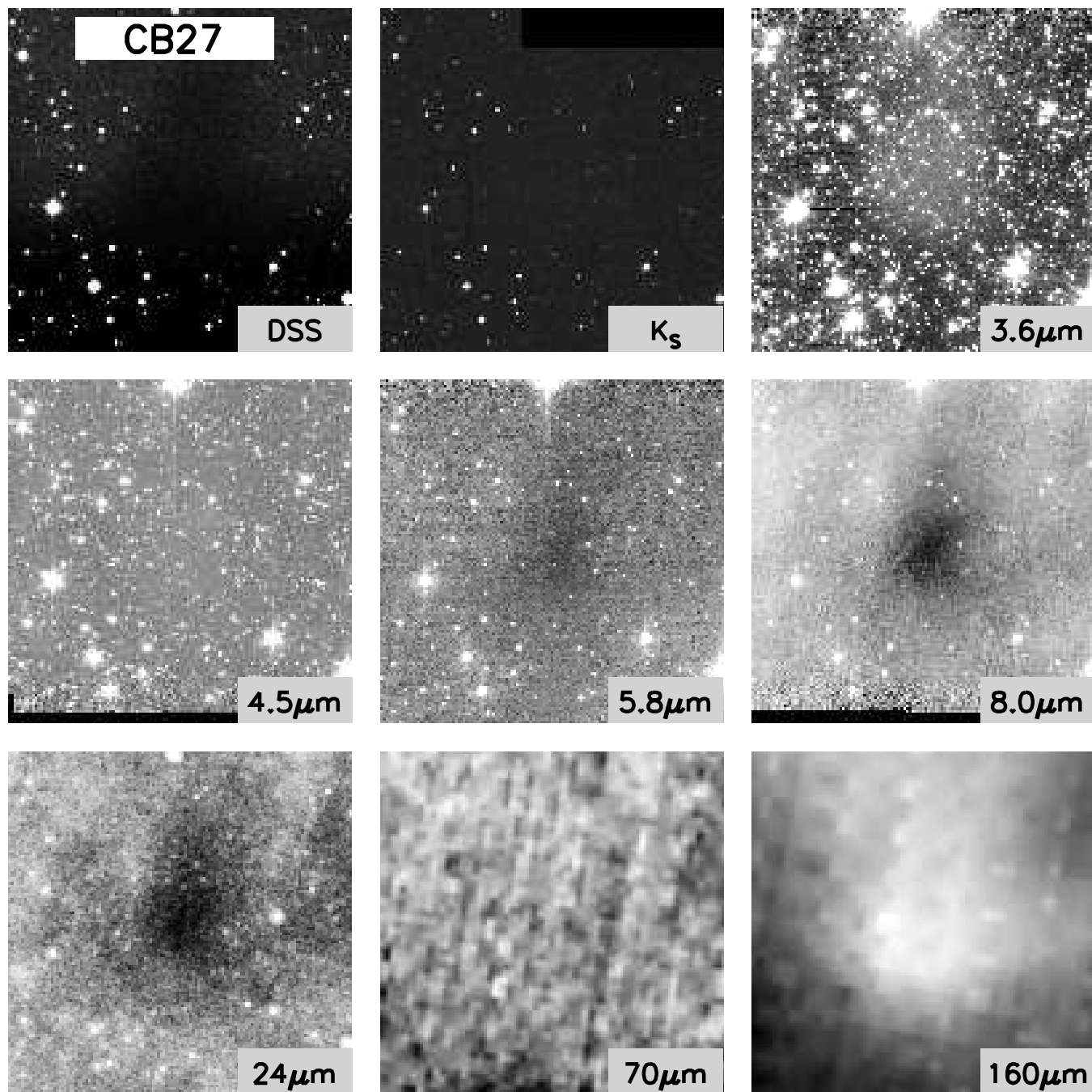


FIG. 4.— Same as Figure 1

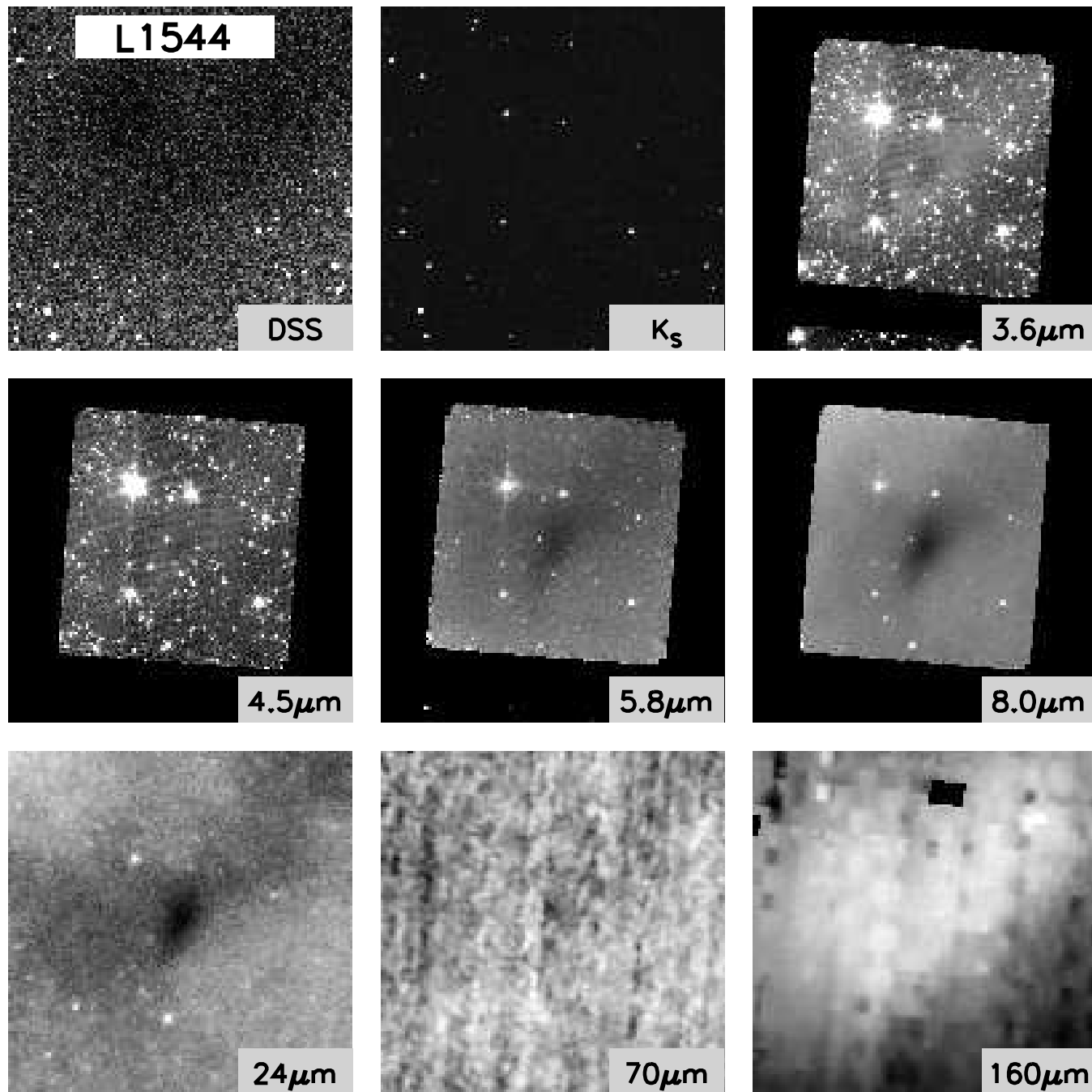


FIG. 5.— Same as Figure 1

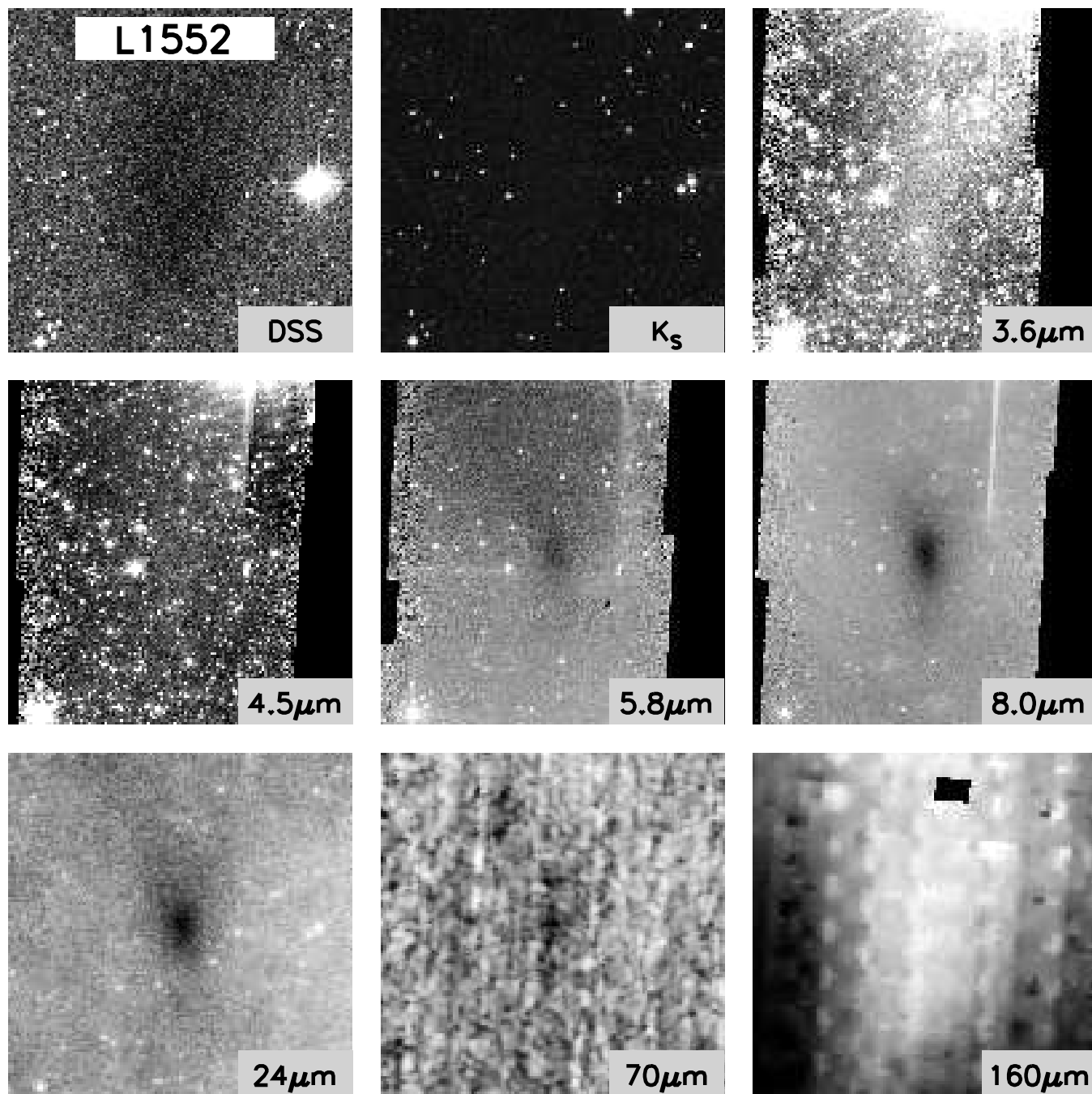


FIG. 6.— Same as Figure 1

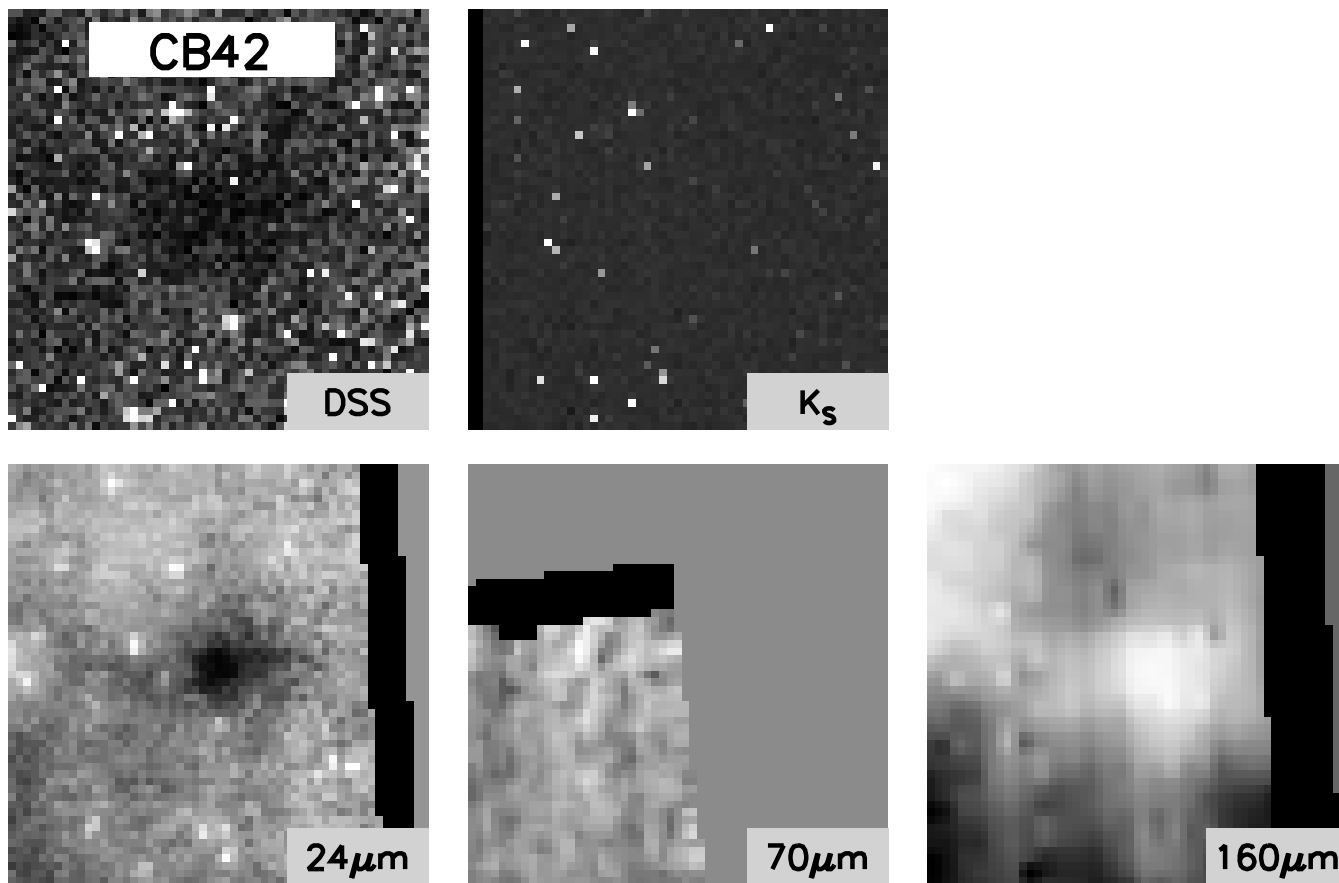


FIG. 7.— Same as Figure 1

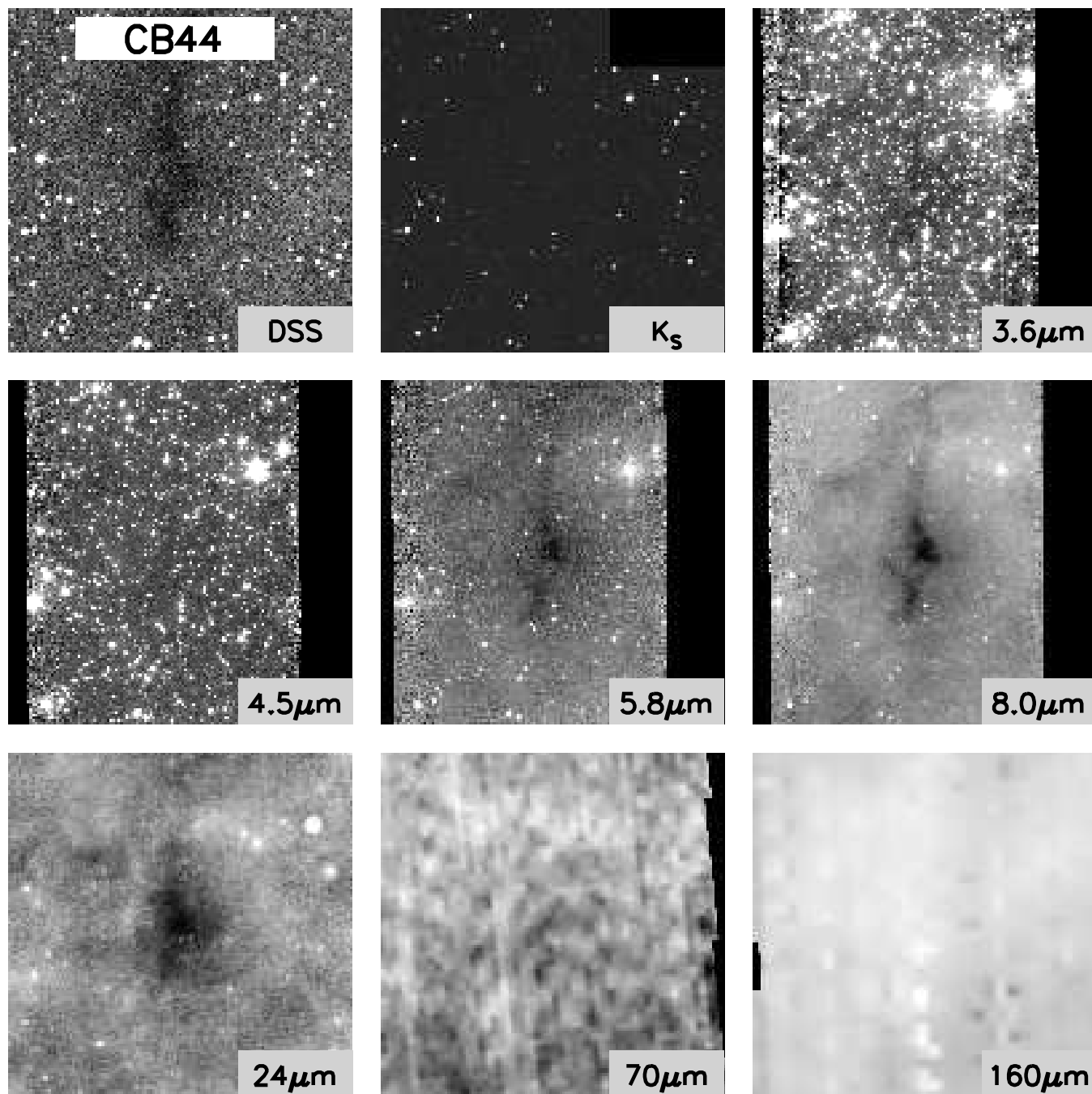


FIG. 8.— Same as Figure 1

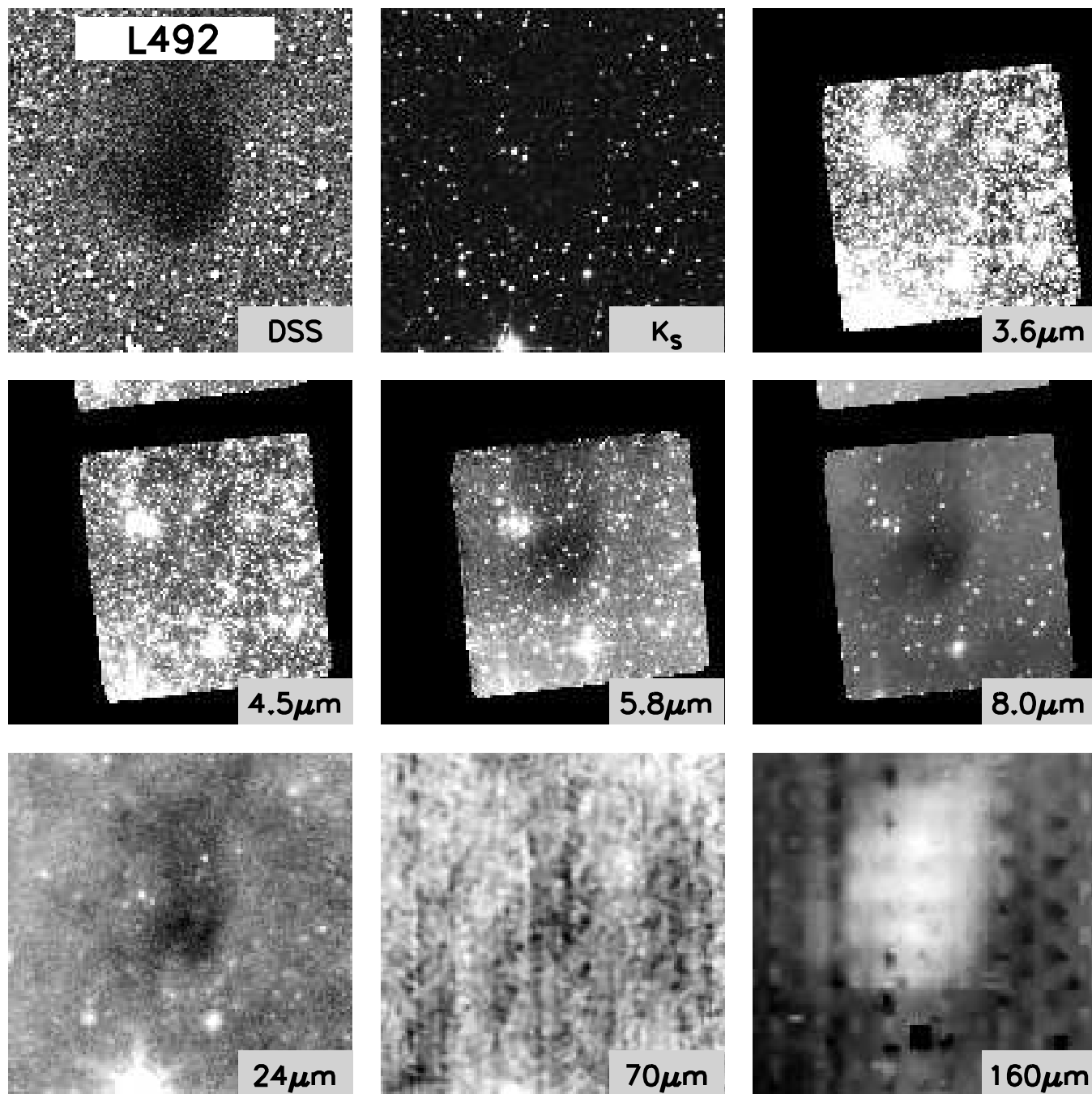


FIG. 9.— Same as Figure 1

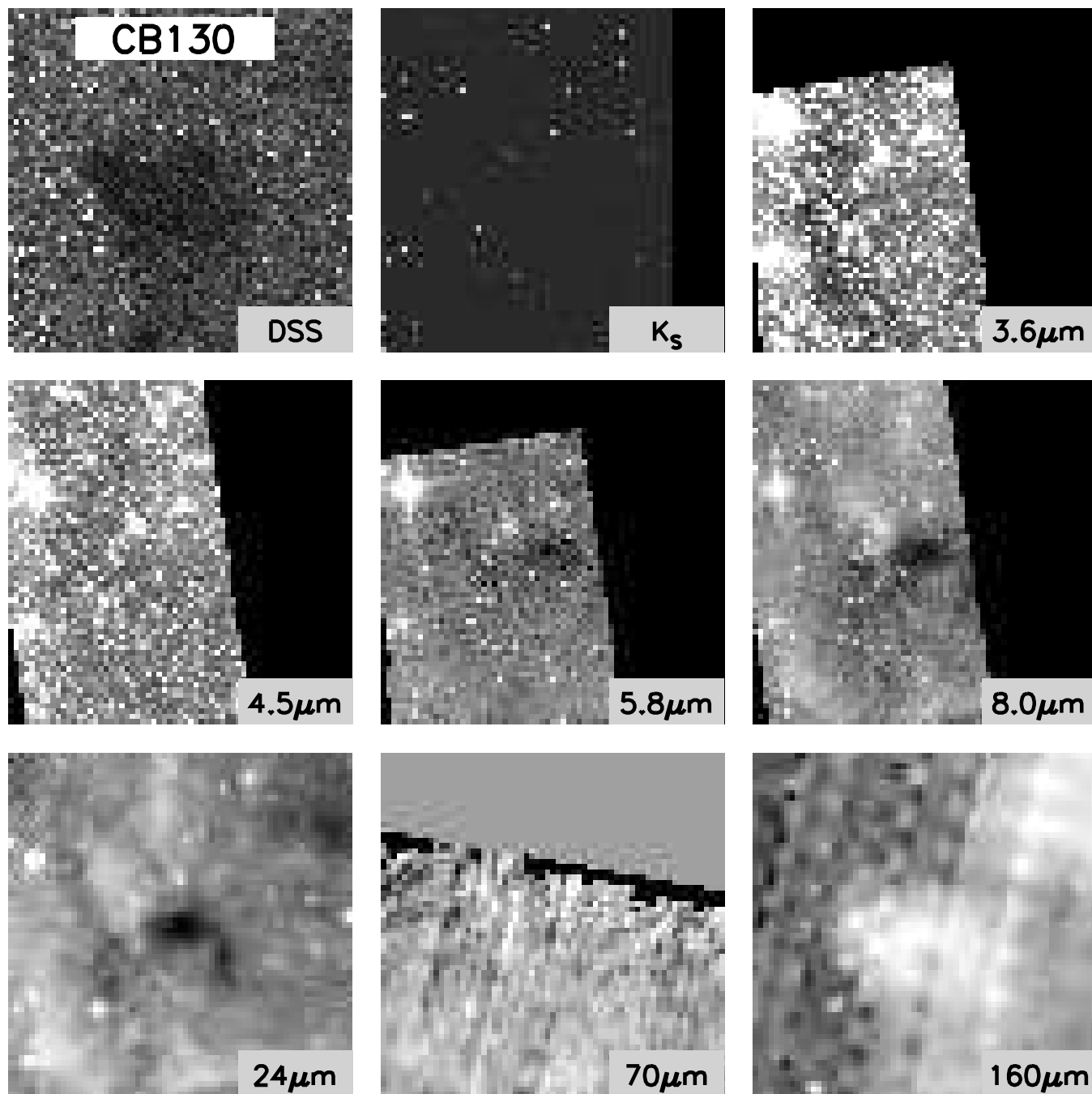


FIG. 10.— Same as Figure 1

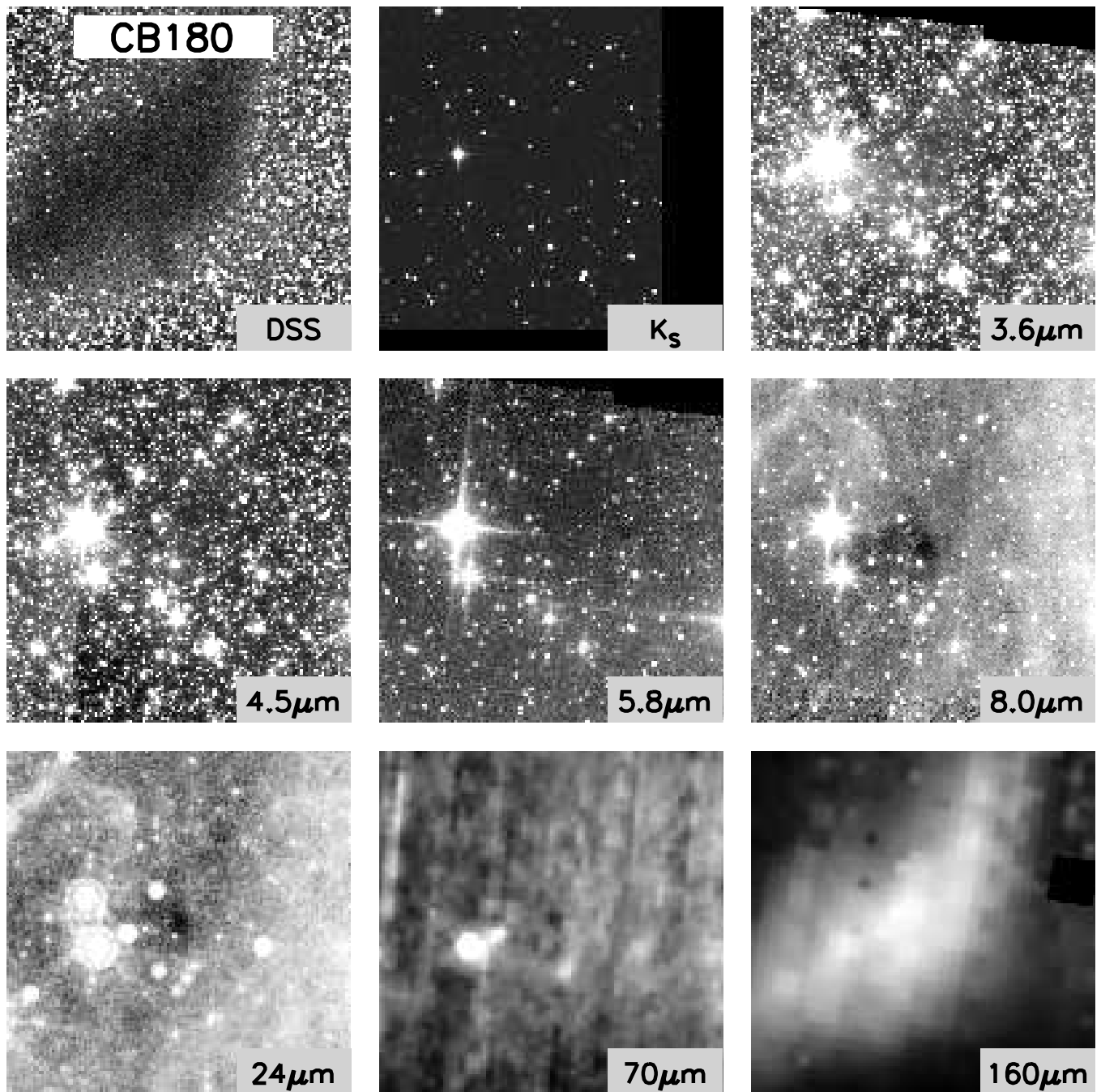


FIG. 11.— Same as Figure 1

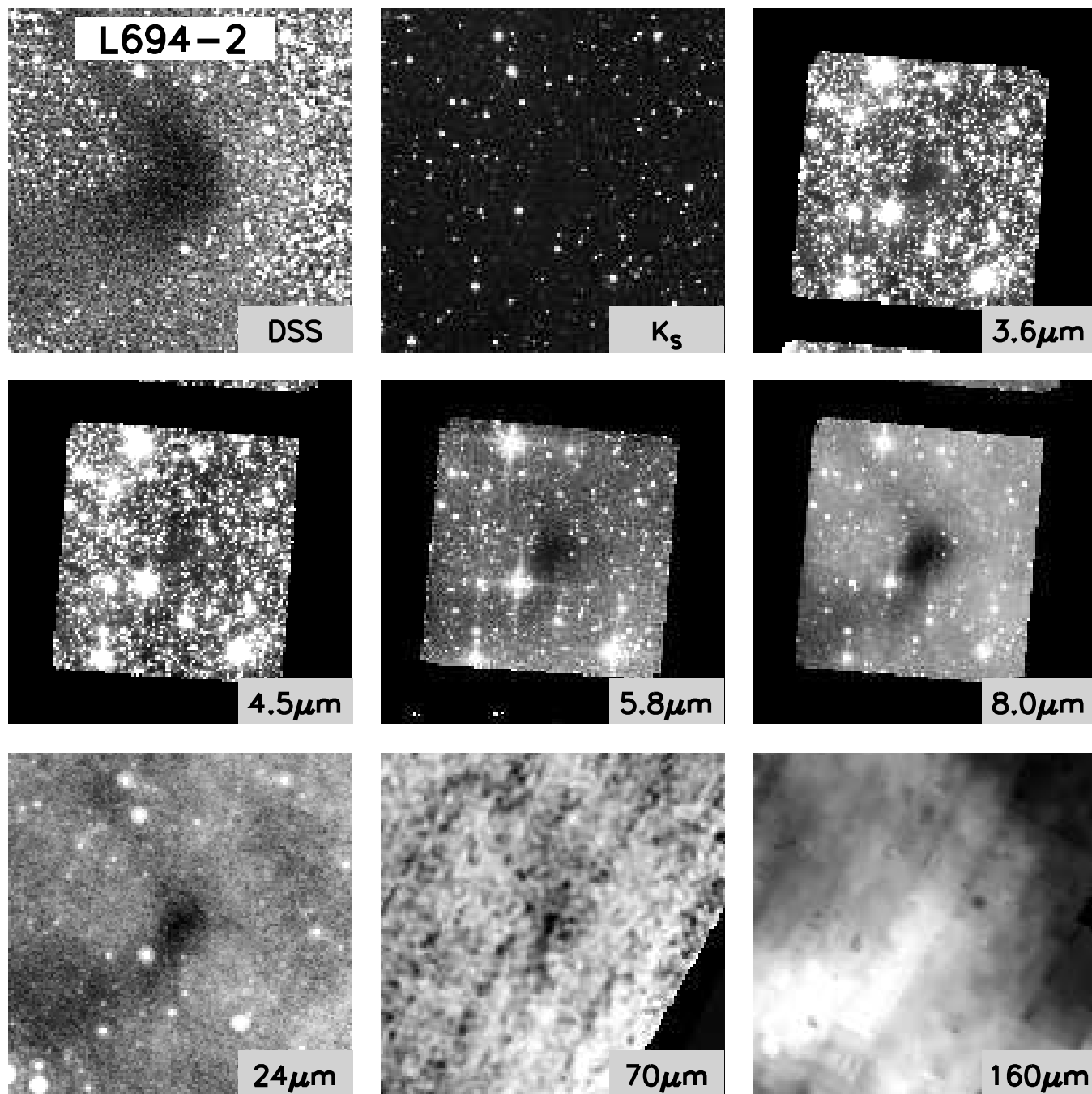


FIG. 12.— Same as Figure 1

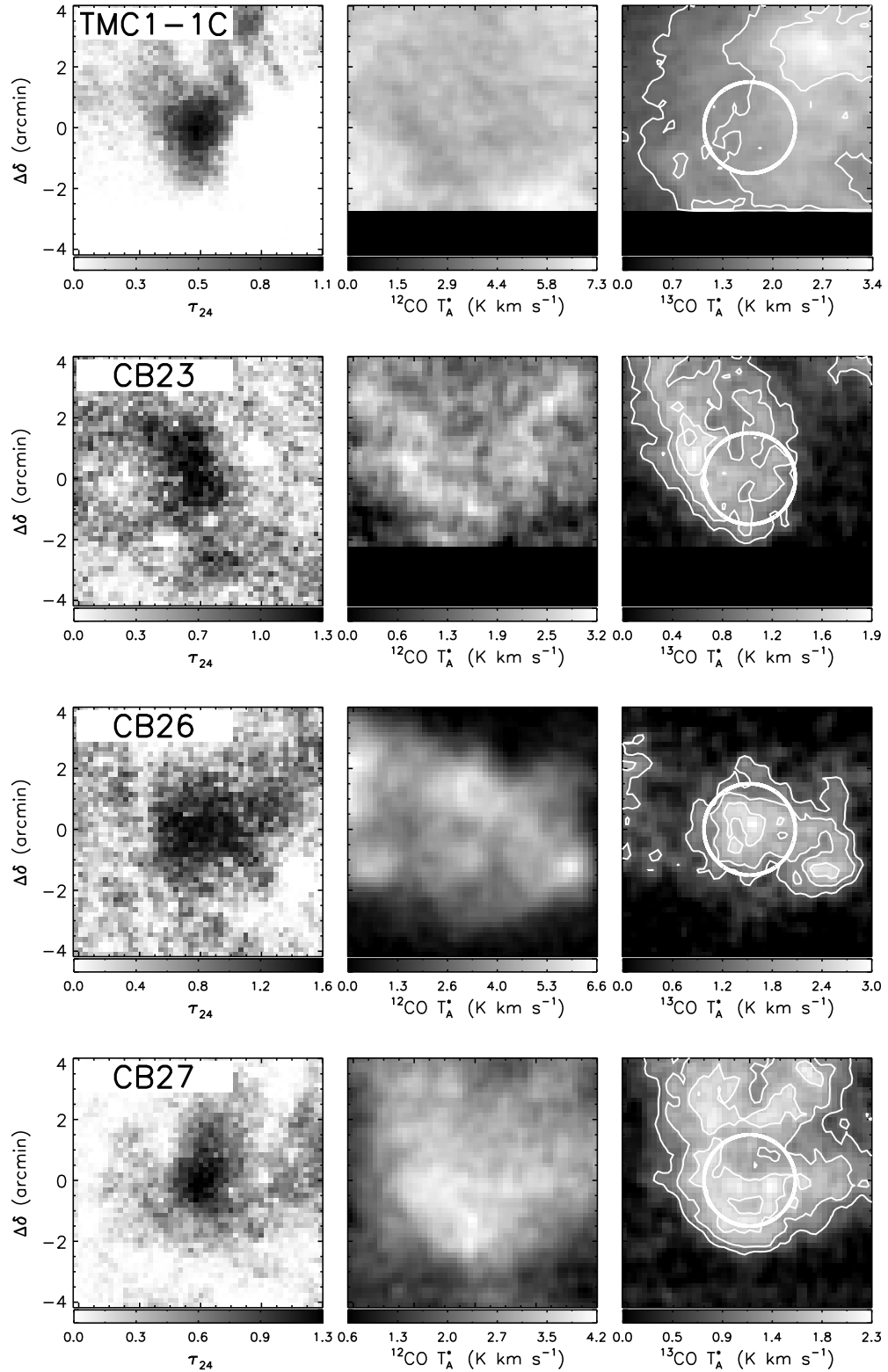


FIG. 13.— τ_{24} -maps and ^{12}CO and ^{13}CO integrated intensity maps, over the velocity ranges listed in Table 2. The black circle ($1''.5$ radius) indicates the area used to calculate the $24\ \mu\text{m}$ shadow masses; the white circle indicates that used to calculate the molecular masses. The ^{13}CO contours levels are 0.4, 0.6, 0.8 times the maximum value indicated in the ^{13}CO color-bar. For full resolution figures contact stutz@mpia.de.

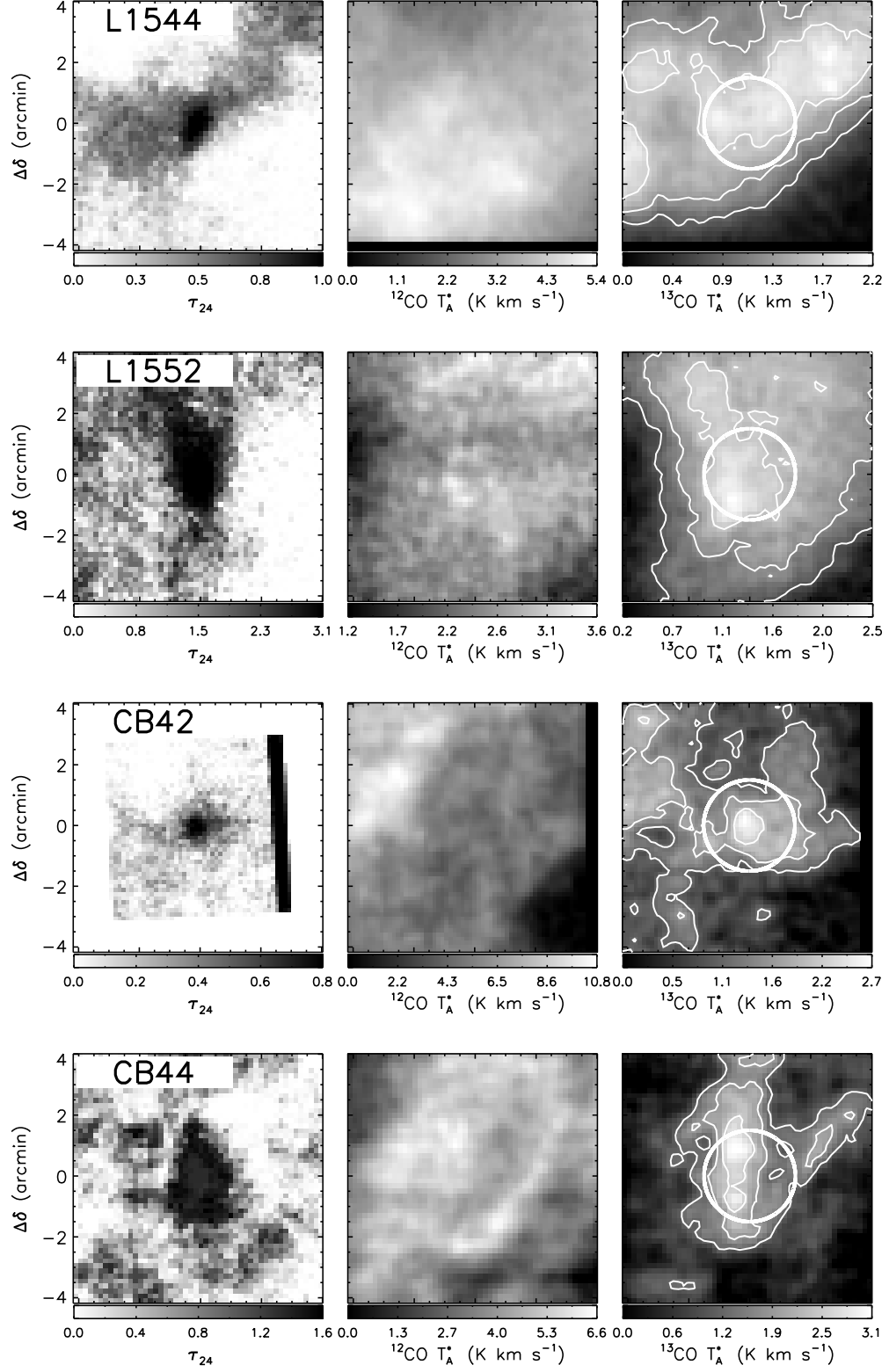


FIG. 14.— Same as Figure 13

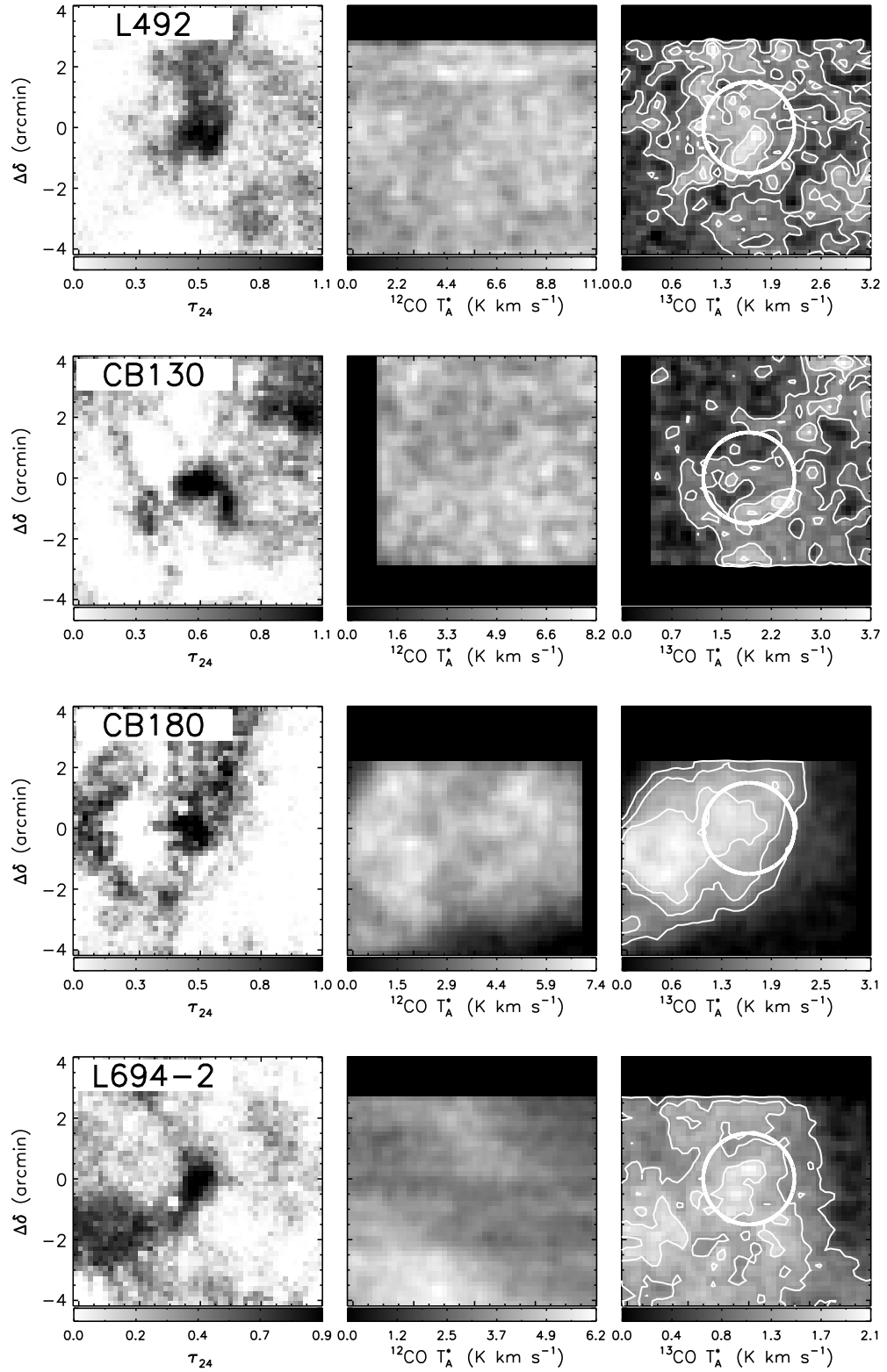


FIG. 15.— Same as Figure 13

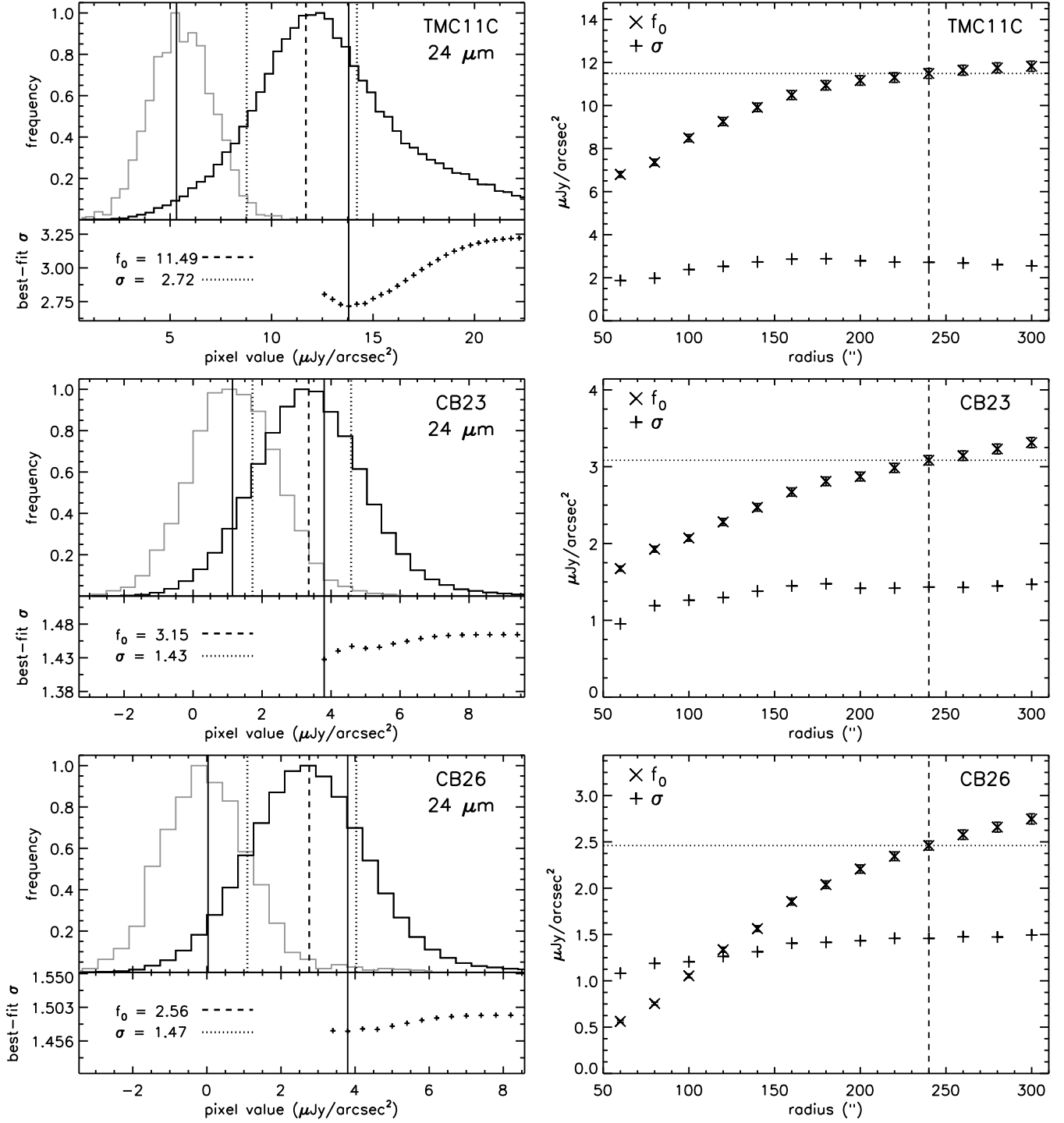


FIG. 16.— *Left Column, top panel* — Black histogram: $24\ \mu\text{m}$ pixel value distribution for background subtracted image region of $r_0 = 240''$ radius (except for CB42), r_0 is indicated in the right column as the dashed line, and is centered on the shadow. Grey histogram: $24\ \mu\text{m}$ pixel value distribution for $30''$ region centered on the shadow. Solid lines: minimum and maximum black histogram bins used to fit for the minimum σ . The dashed line indicates the best-fit mean, or f_0 , value at the minimum best-fit value for σ , indicated by the dotted line. *Left Column, bottom panel* — Best-fit values of σ plotted against the maximum bin value included in the fit. The solid line indicates the minimum value of σ . Best-fit Gaussian parameters σ and the mean (f_0) are indicated. *Right Column*: Best-fit f_0 and minimum σ as a function of aperture size (r_0).

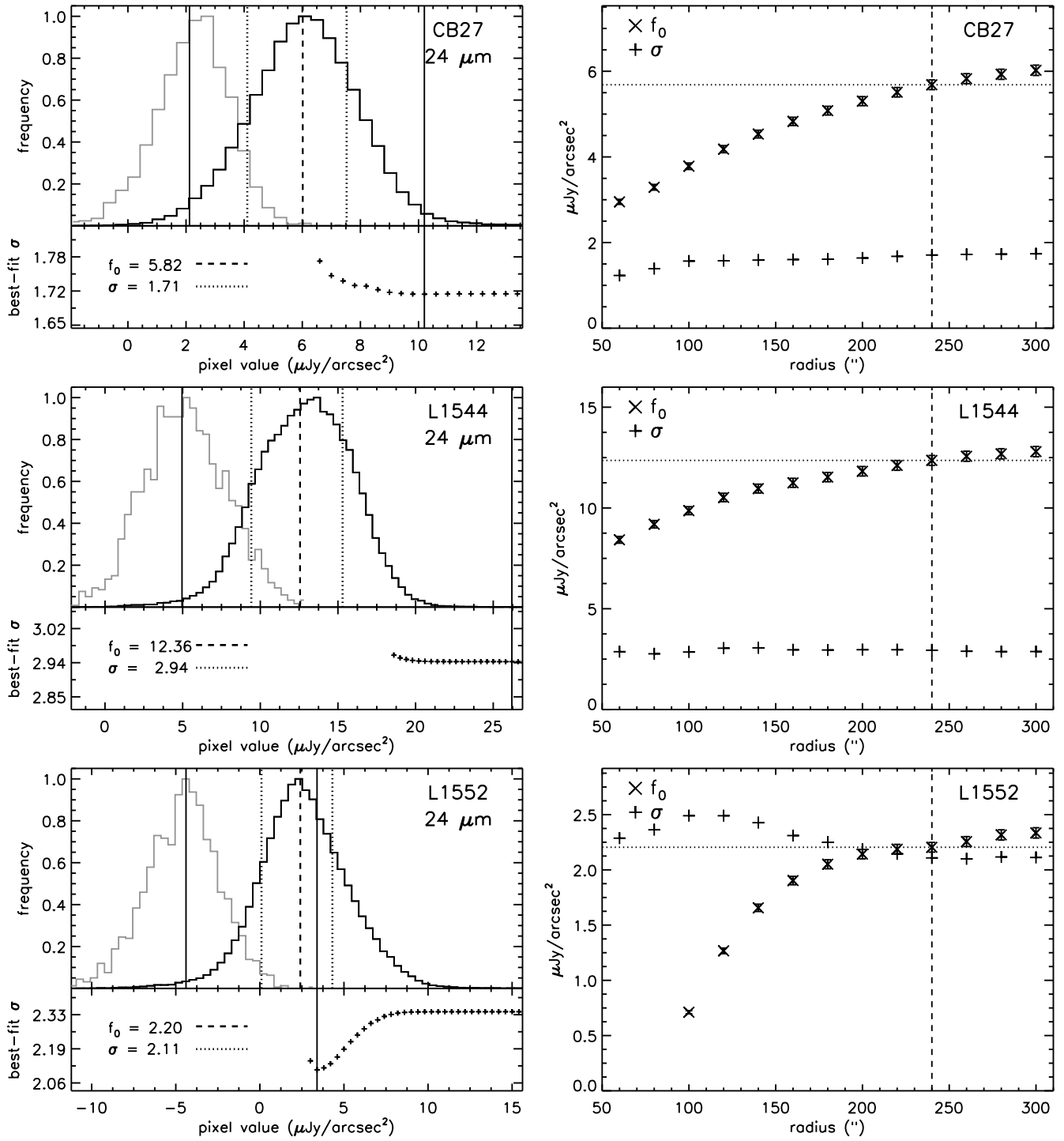


FIG. 17.— Same as Figure 16

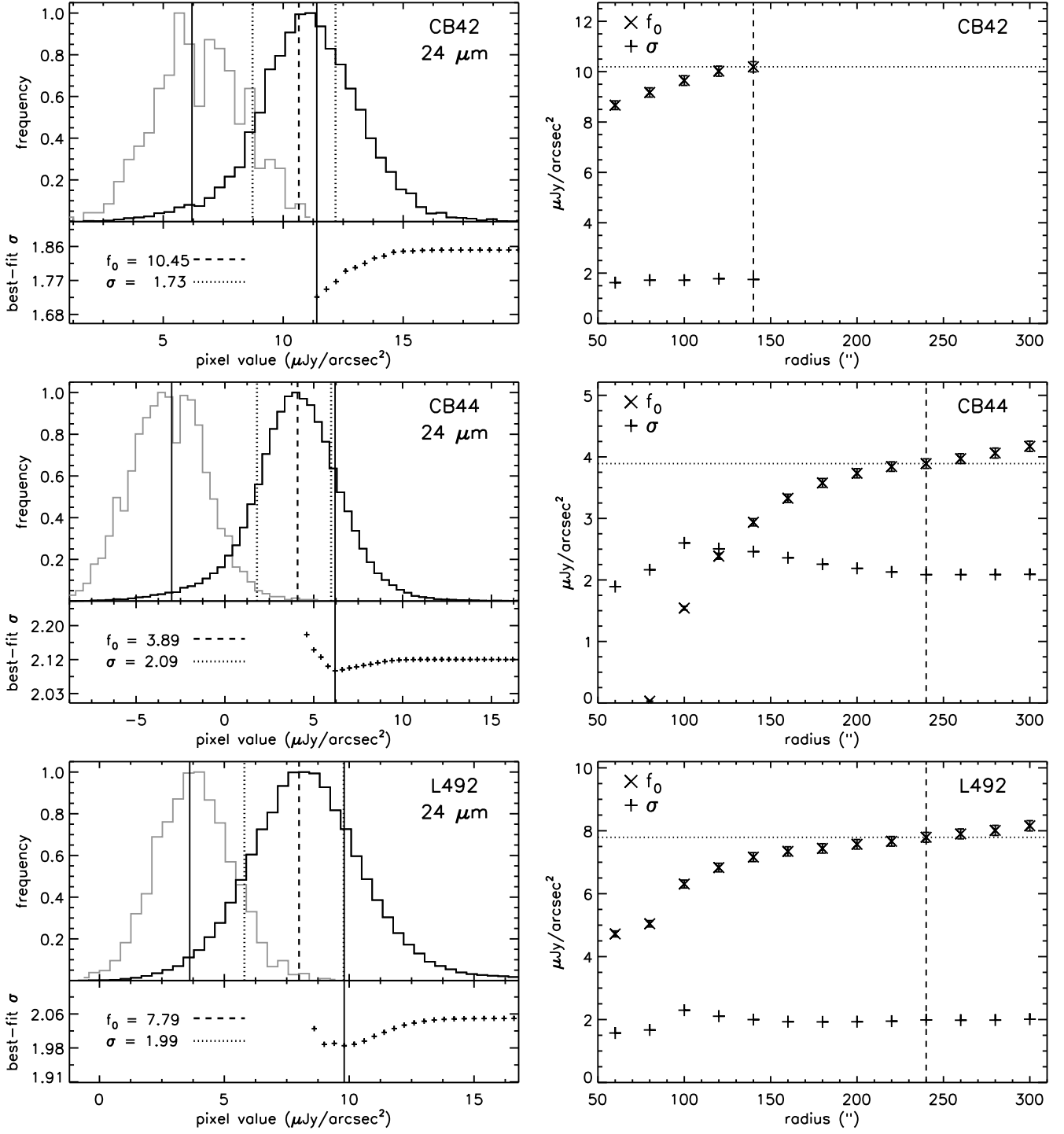


FIG. 18.— Same as Figure 16

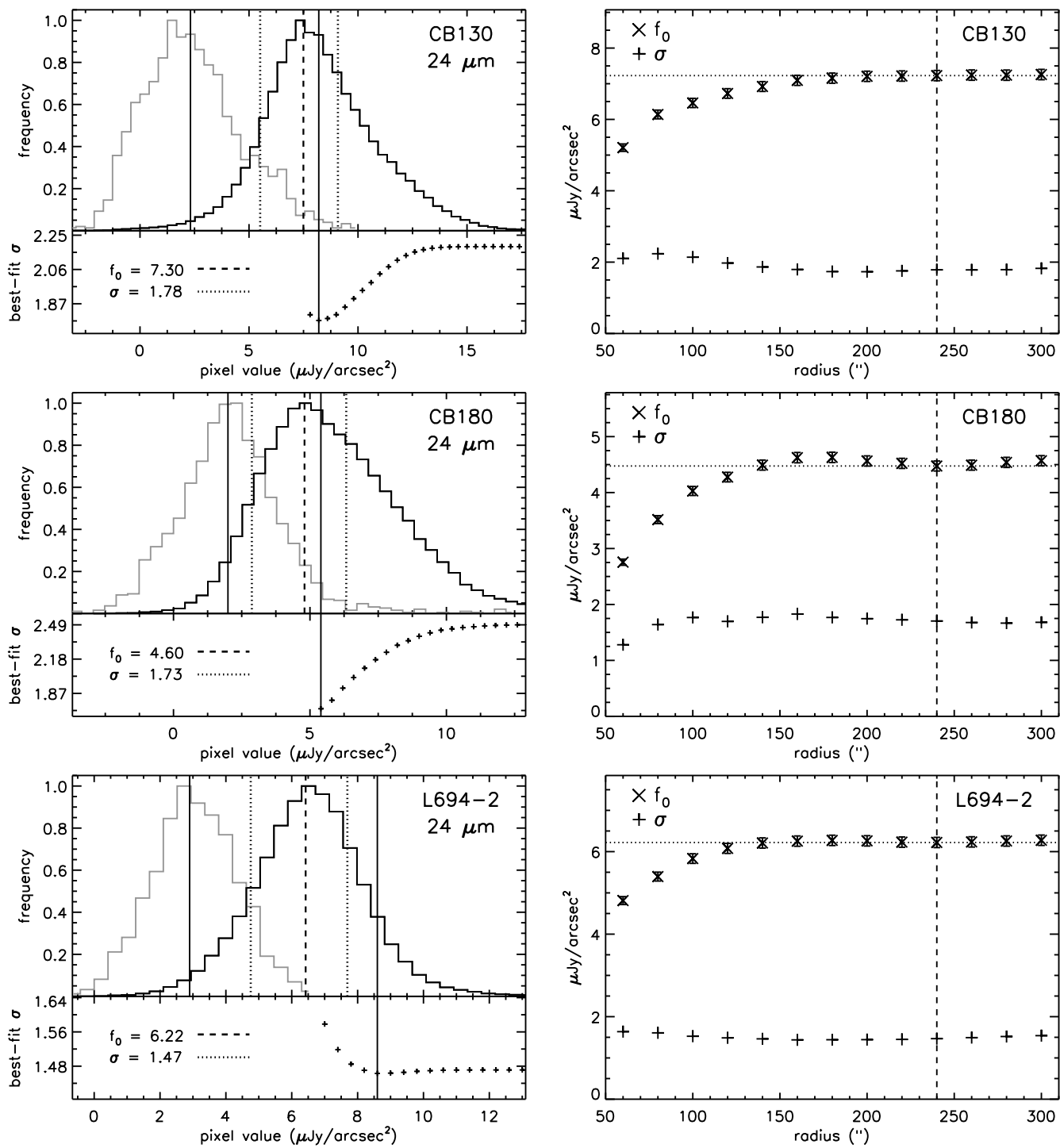


FIG. 19.— Same as Figure 16

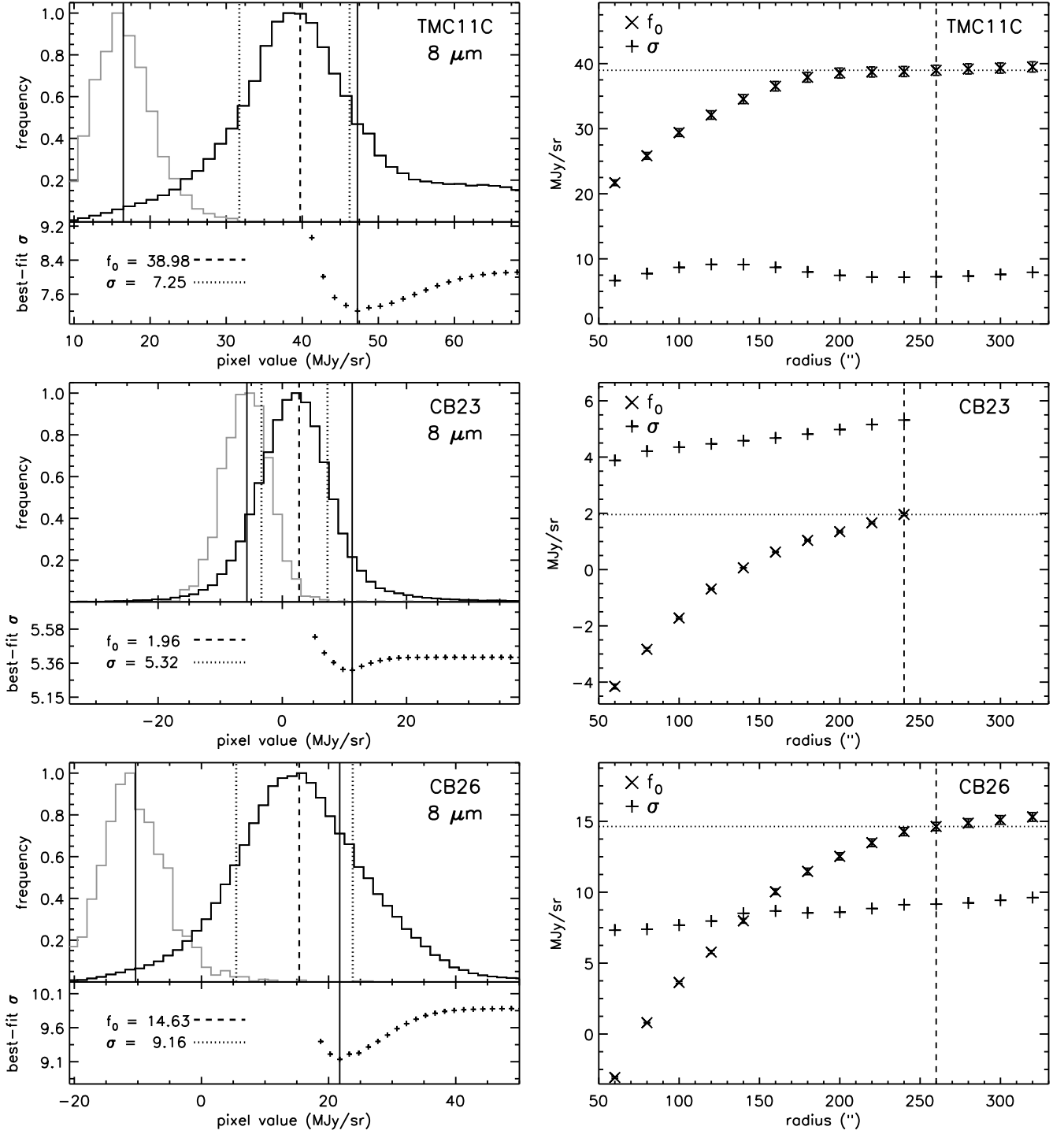


FIG. 20.— *Left Column, top panel* — Black histogram: 8 μm pixel value distribution for background subtracted image region of $r_0 = 240''$ radius (except for CB42), r_0 is indicated in the right column as the dashed line, and is centered on the shadow. Grey histogram: 8 μm pixel value distribution for 30'' region centered on the shadow. Solid lines: minimum and maximum black histogram bins used to fit for the minimum σ . The dashed line indicates the best-fit mean, or f_0 , value at the minimum best-fit value for σ , indicated by the dotted line. *Left Column, bottom panel* — Best-fit values of σ plotted against the maximum bin value included in the fit. The solid line indicates the minimum value of σ . *Best-fit Gaussian parameters σ and the mean (f_0) are indicated.* *Right Column* — Best-fit f_0 and minimum σ as a function of aperture size (r_0).

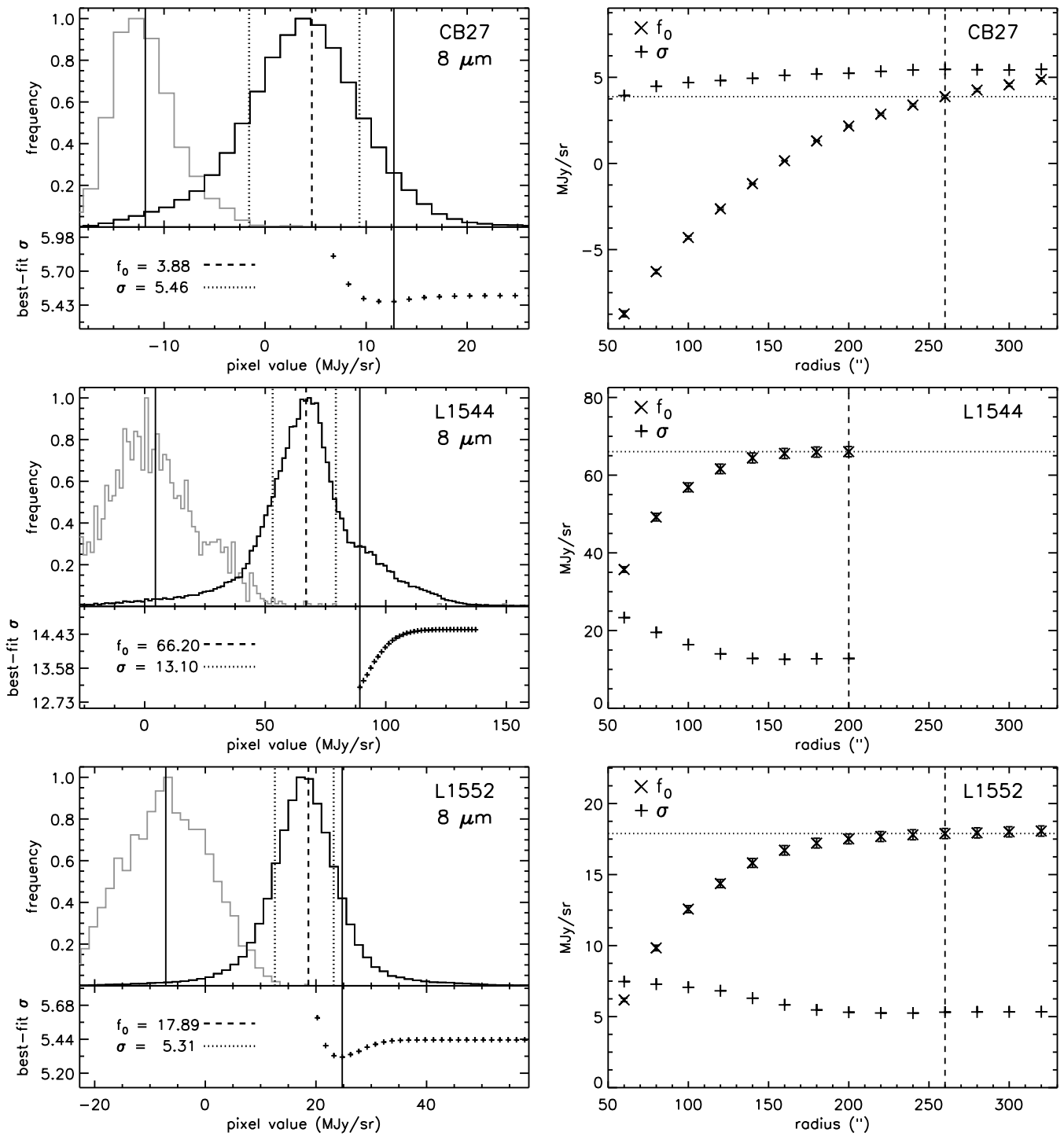


FIG. 21.— Same as Figure 20

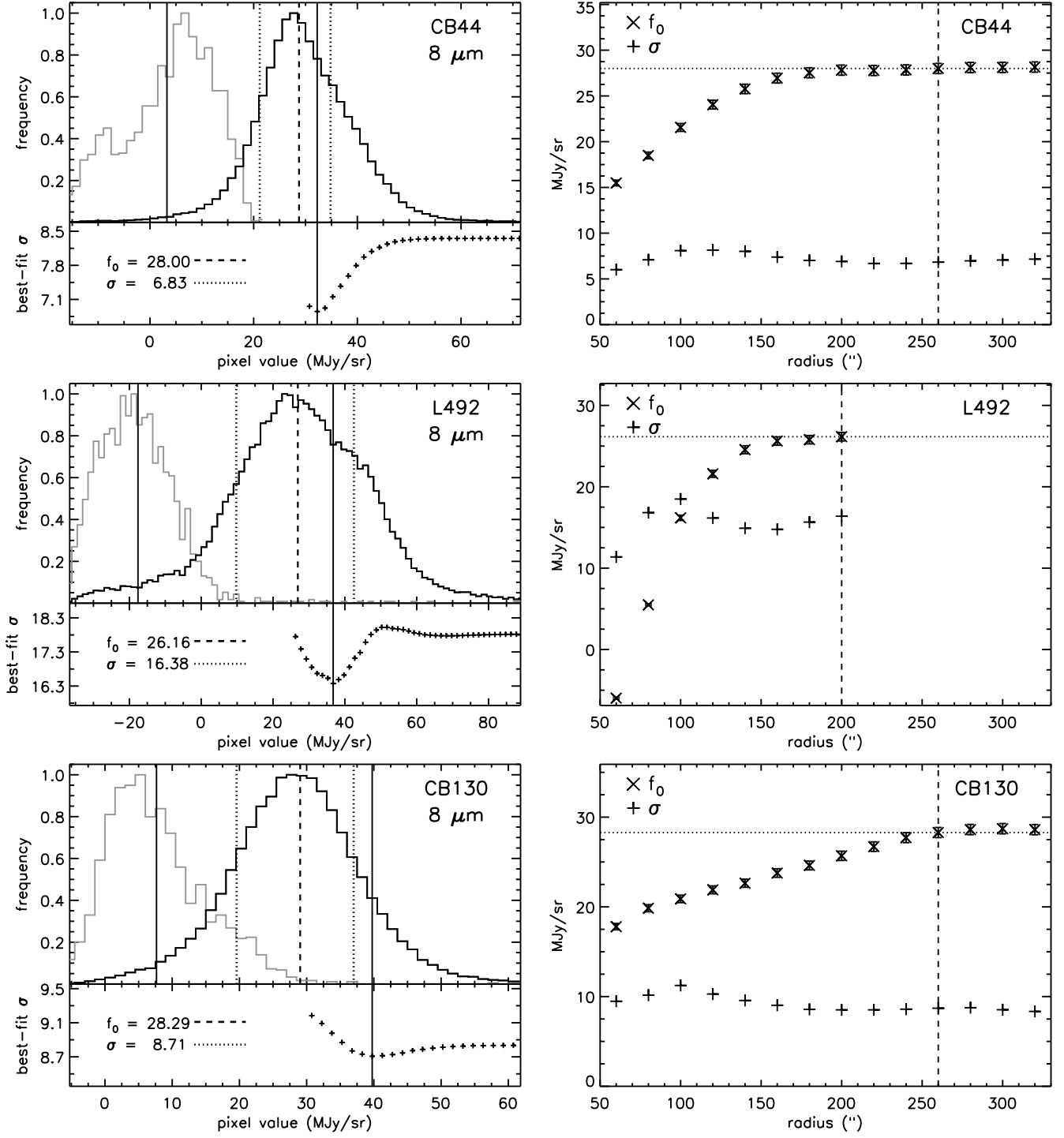


FIG. 22.— Same as Figure 20

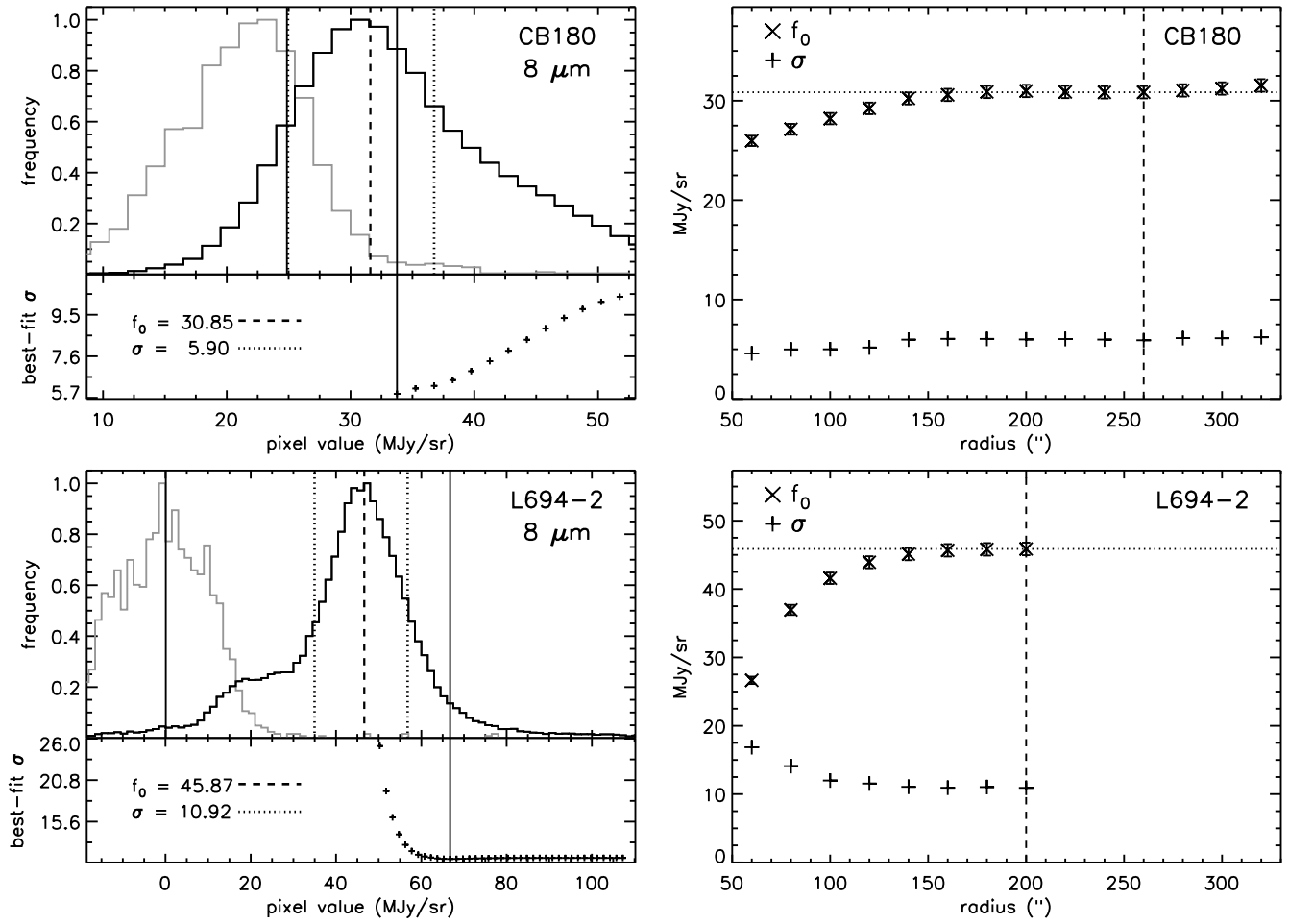


FIG. 23.— Same as Figure 20

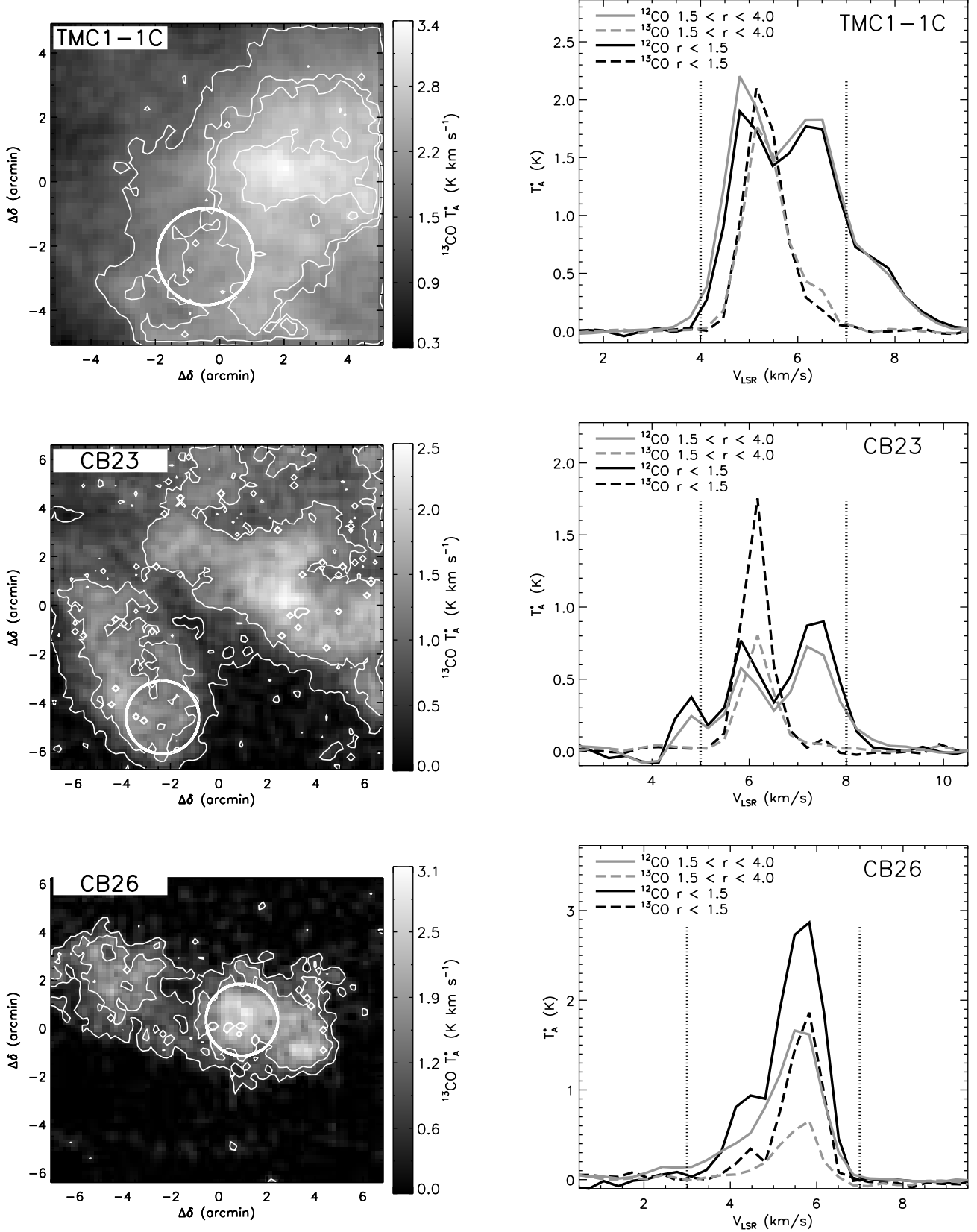


FIG. 24.— *Left Column* — The grey scale image is ^{13}CO (2-1) integrated intensity map. Contours are the CO-model derived $N(\text{H})$ column density maps, which show good spatial agreement between the molecular map; contour levels are scaled to the maximum value of the column density in the region of the shadow. Fractional contour levels for TMC-1C are $\{0.8, 0.9, 0.95, 0.995\} \times 1.19 \times 10^{22} \text{ cm}^{-2}$, for CB23 are $\{0.6, 0.8\} \times 1.09 \times 10^{22} \text{ cm}^{-2}$, and for CB26 are $\{0.5, 0.6\} \times 1.49 \times 10^{22} \text{ cm}^{-2}$. The shadow is indicated by the small white circle, with a radius of $1'.5$; the large circle ($r = 4'.0$) indicates the region in which we calculate mass $M_{\text{CO},4}$ (see Table 4 and text). *Right Column* — Mean ^{12}CO and ^{13}CO spectra for the regions indicated by the circles in the left panel. For full resolution figures contact stutz@mpia.de.

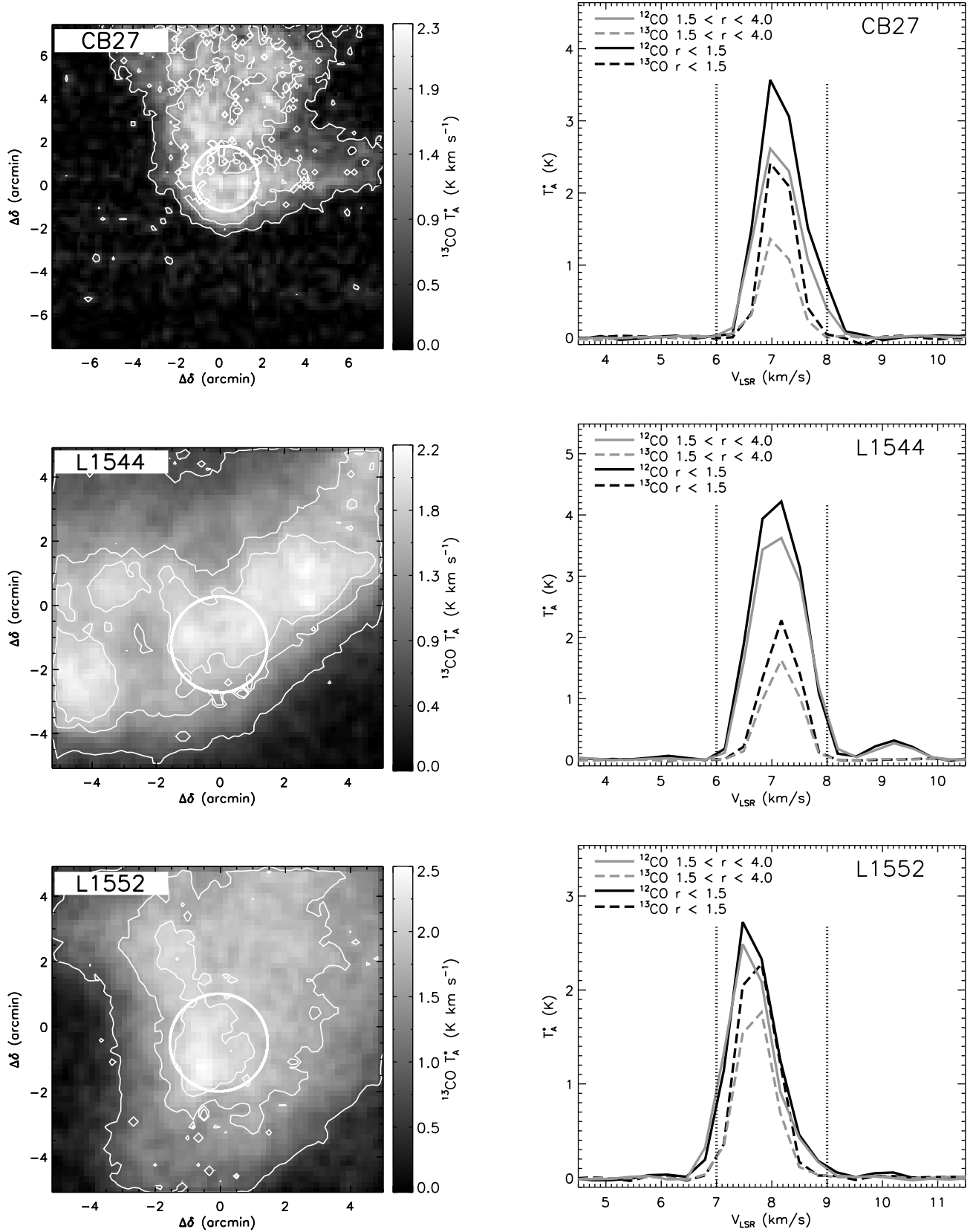


FIG. 25.— Same as Figure 24. Fractional contour levels for CB27 are $\{0.5, 0.7\} \times 1.40 \times 10^{22} \text{ cm}^{-2}$, for L1544 are $\{0.7, 0.9, 0.95\} \times 1.11 \times 10^{22} \text{ cm}^{-2}$, and L1552 are $\{0.7, 0.9, 0.95\} \times 1.15 \times 10^{22} \text{ cm}^{-2}$.

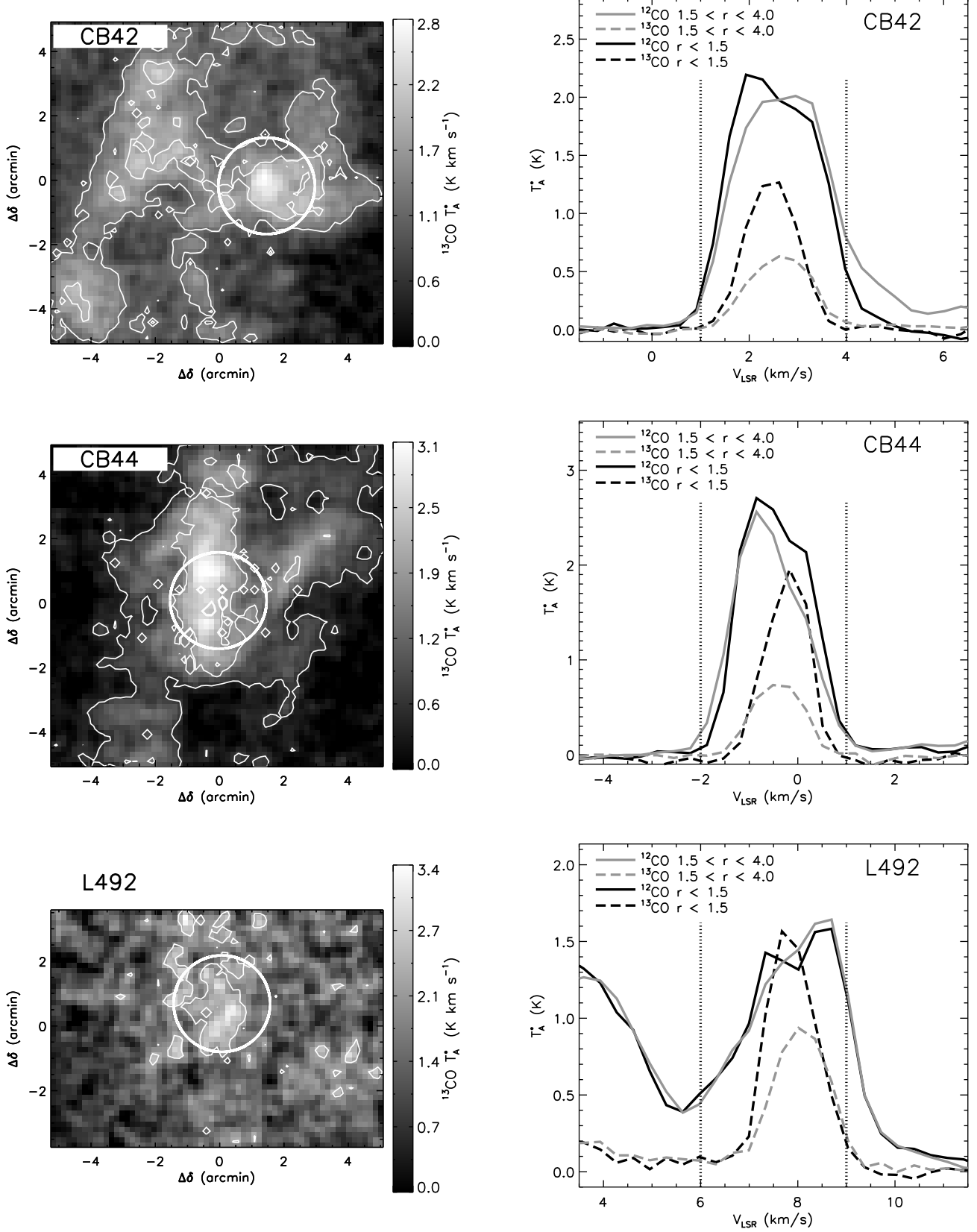


FIG. 26.— Same as Figure 24. Fractional contour levels for CB42 are $\{0.75, 0.85\} \times 1.19 \times 10^{22} \text{ cm}^{-2}$, for CB44 are $\{0.4, 0.55\} \times 1.86 \times 10^{22} \text{ cm}^{-2}$, and L492 are $\{0.85\} \times 1.24 \times 10^{22} \text{ cm}^{-2}$.

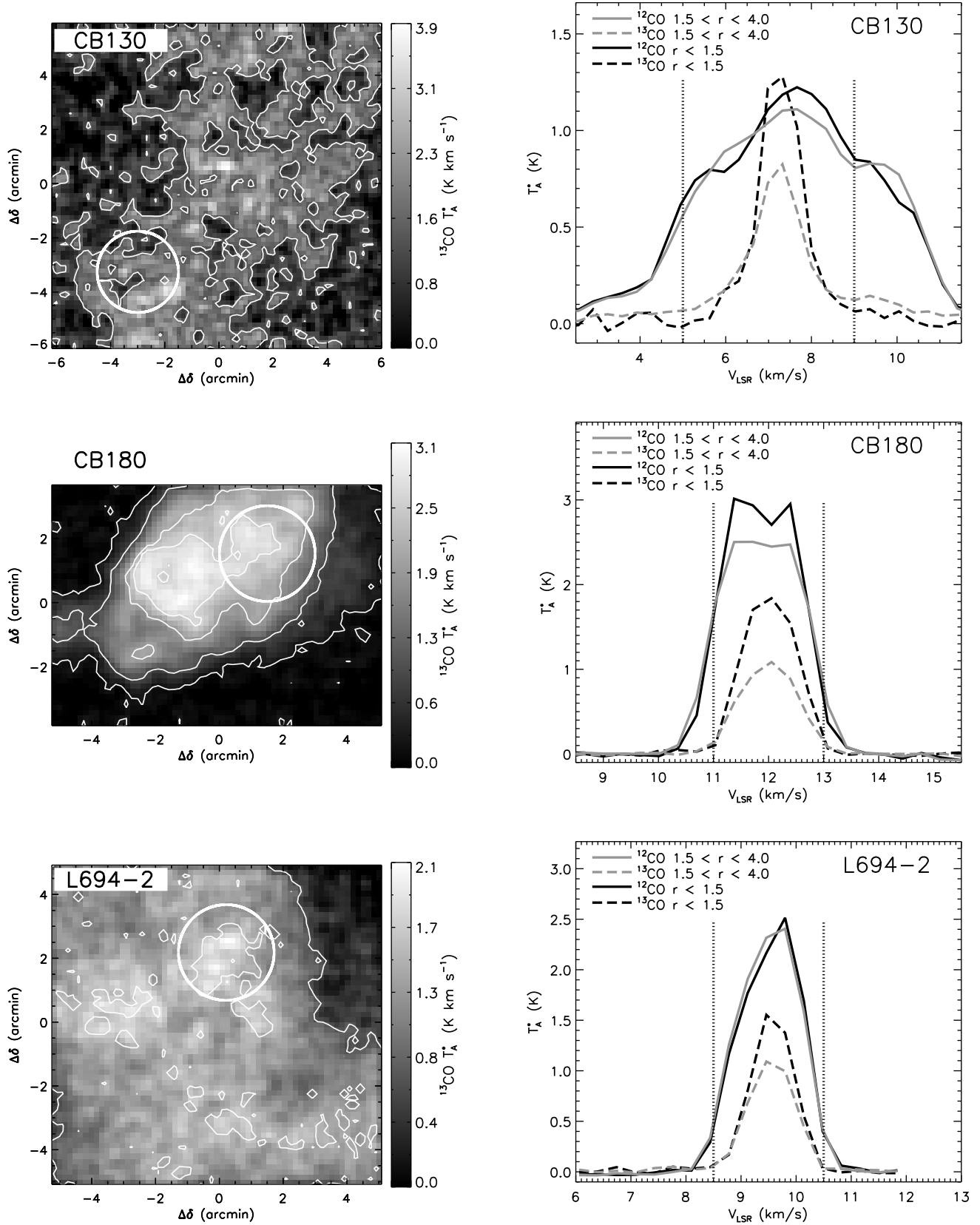


FIG. 27.— Same as Figure 24. Fractional contour levels for CB130 are $\{0.75\} \times 1.21 \times 10^{22} \text{ cm}^{-2}$, for CB180 are $\{0.5, 0.7, 0.9, 0.97\} \times 1.21 \times 10^{22} \text{ cm}^{-2}$, and L694-2 are $\{0.7, 0.9\} \times 1.11 \times 10^{22} \text{ cm}^{-2}$.

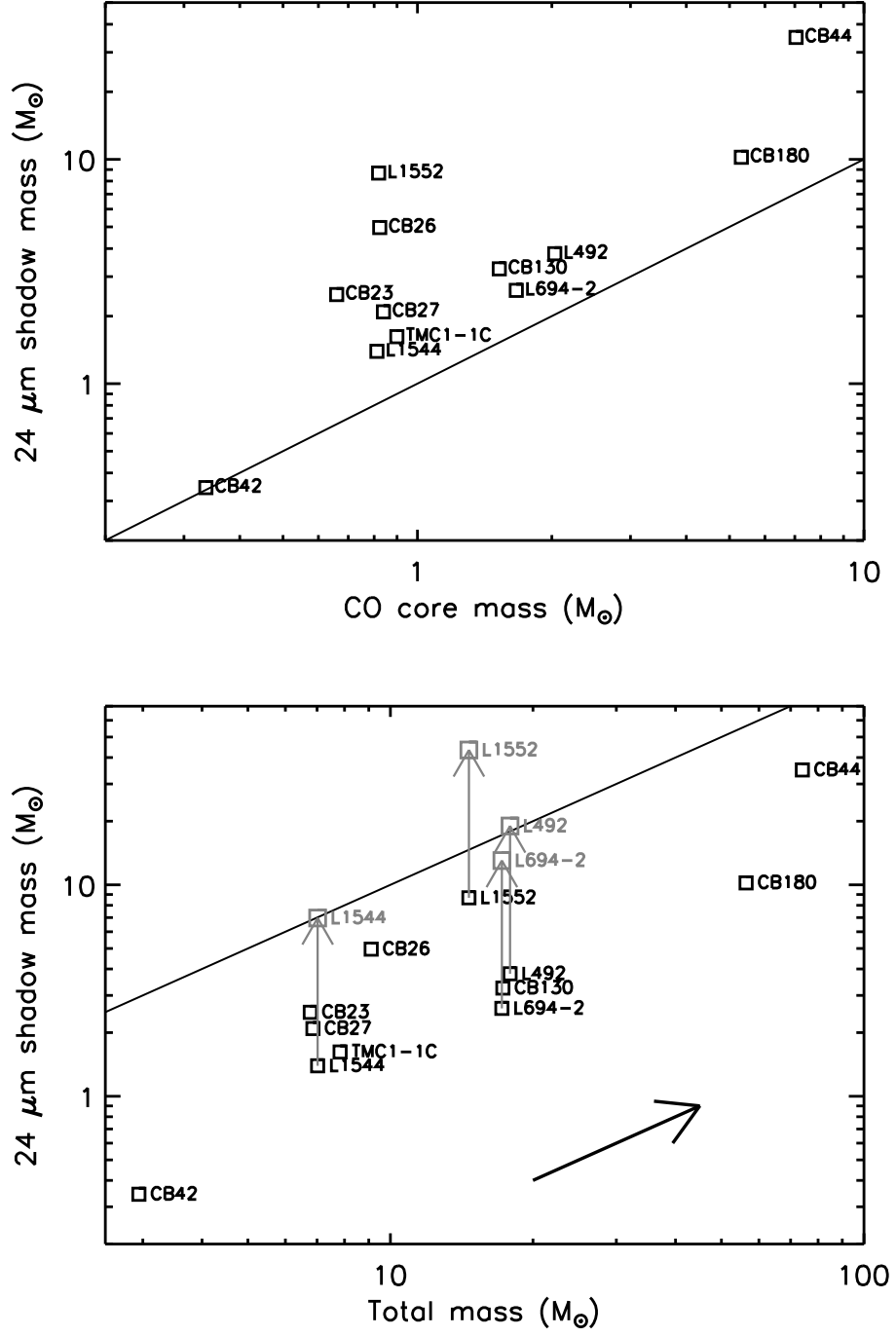


FIG. 28.— Masses presented Table 4 are plotted here. *Top panel* — The CO core masses calculated over the area of the core are plotted versus the 24 μm shadow masses. *Bottom panel* — The total masses ($M_{\text{CO},4} + M_{24}^{\text{core}} - M_{\text{CO}}^{\text{core}}$) are plotted versus the 24 μm shadow masses. The arrow indicates the effect of 50% change in the assumed distance. In both panels the black curve indicates equality between the ordinate and the abscissa.